Development of Chlorophyll-a and Total Suspended Solids Algorithms for Monitoring Water Quality in the Inanda Dam, KwaZulu-Natal, Using Remotely Sensed Landsat 8 and Sentinel 2 Imagery

Report to the
Water Research Commission

by

Dr SN Njoya and V Moodley
School of Agriculture, Earth and Environmental Science,
University of KwaZulu-Natal, Howard Campus

WRC Report No. 2918/1/22
ISBN 978-0-6392-0338-6

April 2022

Obtainable from
Water Research Commission
Private Bag X03
Gezina
PRETORIA, 0031

orders@wrc.org.za or download from www.wrc.org.za

EXECUTIVE SUMMARY

Freshwater resources are crucial for all life on Earth. Water is necessary for drinking, agriculture, industries, socio-economic development, and more. The maintenance and balance of ecosystems are also dependent on water to a large extent. However, water quality has declined considerably due to anthropogenic activities. Therefore, it is imperative to monitor and manage inland water bodies to ensure their supply quantity and quality. Traditionally, monitoring water quality is time-consuming and labour-intensive, expensive, and inaccessible in certain areas. New efficient and cost-effective methods now need to be employed to monitor freshwater resources. Remote sensing, the art of acquiring information about the planet from a distance, can monitor water quality.

This study looked at the ability of Landsat 8 and Sentinel 2 to monitor water quality in the Inanda Dam, Durban, KwaZulu-Natal (KZN) Province. The aim was to develop algorithms to retrieve chlorophyll-a (chl-a) and total suspended solids (TSS) from Landsat 8 and Sentinel 2 imagery and produce their surface distribution in the Inanda Dam. This report consists of five chapters:

1. Background Information
2. Literature Review
3. Methodology
4. Results and Discussion
5. Conclusions and Recommendations

Chapter one contains background information on the status of water quality globally, monitoring water quality in-situ and via remotely sensed imagery, the project aims and objectives, and limitations of the study.

Chapter two is a literature review that includes information on the global status of water quality, Landsat 8 and Sentinel 2 satellites, different atmospheric correction methods, different mathematical methods available to generate algorithms, and water quality in the South African context. The literature review revealed that while many studies have been conducted internationally on remotely sensed chl-a and TSS, little has been done in South Africa and studies are ongoing. Pre-processing of satellite imagery is often conducted, and the most popular method of algorithm development is via empirical formulas. The results of previous studies on the development of algorithms for monitoring water quality are varied; however, there is a general agreement that chl-a and TSS can be estimated from Landsat 8 and Sentinel 2.

Chapter three describes the study's methodology, including in-situ sampling for chl-a and TSS concentrations, extraction of radiance and reflectance data from satellite imagery, algorithm development using in-situ chl-a/TSS and remote sensing radiance and reflectance data, and the production of chl-a/TSS surface distribution maps.

Chapter four presents and discusses the results obtained from this study. In the results, Landsat 8 bands 1, 2 and 4, and Sentinel 2 bands 1 and 3 correlated well with in-situ chl-a, while Landsat 8 band 1 and Sentinel 2 bands 1 and 3 correlated best with in-situ TSS. These bands were used to develop algorithms that successfully estimated chl-a and TSS concentrations in the Inanda Dam. Surface distribution maps were developed from the most successful algorithms, showing the trend of chl-a and TSS in the Dam. The results of this study support the findings of studies conducted internationally, which indicate that chl-a and TSS can be estimated from both Landsat 8 and Sentinel 2 imagery.

Chapter five presents the conclusions and recommendations of this study and suggestions for future studies. A key finding of this study was that chl-a and TSS could be successfully retrieved from Landsat 8 and Sentinel 2 imagery. The developed algorithms captured and mapped the surface distribution of chl-a and TSS in the Inanda Dam. It is recommended that more research be conducted in many dams across South Africa to enable

comparisons, possible synthesis and to expand the body of existing knowledge on remote sensing and water quality.

ACKNOWLEDGEMENTS

The project team wishes to thank the following people for their contributions to the project.

Reference Group	Affiliation
Dr E Ubomba-Jaswa	Water Research Commission
Dr MA Mohamed Ahmed	Sol Plaatje University
Prof. A Ramoelo	University of Pretoria
Dr S Madonsela	Council for Scientific and Industrial Research
Dr MW Matthews	CyanoLakes

This page was intentionally left blank

CONTENTS

LIST OF FIGURES

LIST OF TABLES

ACRONYMS & ABBREVIATIONS

ANN	Artificial Neural Networks
BOA	Bottom of Atmosphere
CDOM	Coloured Dissolved Organic Matter
Chl-a	Chlorophyll-a
CR2CC	Case 2 Regional Coast Colour
DN	Digital Numbers
DOC	Dissolved Organic Carbon
DOS	Dark Object Subtraction
DP	Darkest Pixel
EC	Electric Conductivity
ESA	European Space Agency
FLAASH	Fast Line-of-sight Atmospheric Analysis of Hypercubes
IOP	Inherent Optical Properties
KZN	KwaZulu-Natal
LaSRC	Landsat 8 Surface Reflectance Code
MERIS	Medium Resolution Imaging Spectrometer
Mob-ELM	Model-Based Empirical Line Method
MUMM	The Management Unit of the North Seas Mathematical Models
QAC	Quick Atmospheric Correction
R	Pearson Correlation
R^2	Correlation of Determination
SDD	Secchi Disk Depth
SE	Standard Error
TN	Total Nitrogen
TOA	Top Of Atmosphere
TP	Total Phosphorous
TSS	Total Suspended Solids
USGS	United States Geological Survey
6S	Second Simulation of Satellite Signal in the Solar Spectrum

GLOSSARY

TERM	MEANING
Atmospheric correction	A method used to remove the scattering and absorption effects from the atmosphere to obtain the surface reflectance characterizing surface features.
BOA reflectance	This represents the actual reflectance of the features on the surface of the Earth. The BOA values are calculated from the TOA values by using a physical model (Sen2Cor tool for Sentinel-2), with an attempt to eliminate the effect of the atmosphere on the reflectance values.
Digital Numbers	Represents the amount of energy reflected or emitted by features and captured by a sensor in a particular region of the electromagnetic spectrum.
Geospatial data	Data or information that has a geographic component.
In-situ	Collection of samples at a site.
Radiance	The flux of energy leaving a feature and measured by remote sensing instruments.
Radiometric correction	Refers to a range of processes to correct for sensor irregularities and unwanted sensor or atmospheric noise; and the conversion of digital numbers from satellite or aerial sensors to a common physical scale based on known reflectance measurements taken from objects on the ground's surface. This type of correction is important for reliable quantitative measurements from imagery.
Radiometric resolution	The smallest observable difference in energy. Also, defined as the ability of a sensor to distinguish different grey-scale values. It is measured in bits. The more bits an image has, the more grey-scale values can be stored, and, thus, more differences in the reflection on the land surfaces can be spotted.
Reflectance	The ratio of the amount of light leaving a target to the amount of light incident on a target.
Spatial resolution	The size of the smallest feature that can be detected by a satellite sensor or displayed in a satellite image.
Spatial-temporal	Geographic or spatial data or information collected across time and space.
Spectral signatures	The variation of reflectance or emittance of a material.
Temporal resolution	The amount of time needed by a sensor to revisit and acquire data for the same location.
TOA reflectance	Represents the "raw" reflectance of earth's features as measured from space.

CHAPTER 1: BACKGROUND

1.1 INTRODUCTION

Monitoring water quality is vital to ensure the sustainability of limited freshwater resources globally. Freshwater resources are essential for the functioning of terrestrial ecosystems and to support anthropogenic services such as domestic use, agriculture, industrialization, waste disposal, and drinking water (Lim and Choi, 2015; Bonansea et al., 2019; Soomets et al., 2020; Hu et al., 2021). Unfortunately, these special freshwater functions and services are continually impacted by increasing population and economic development, leading to eutrophication, pollution, brownification, nutrient enrichment, and the overall degradation of freshwater resources (Chen et al., 2021; Ledesma et al., 2019; Ouma et al., 2020; Hu et al., 2021).

Water quality is traditionally monitored using in-situ point sampling methods, which are expensive, time-consuming, labour intensive, and cannot be performed in areas that are difficult to access. In addition, these methods cannot capture the spatial variation of water quality parameters in a water body (Zhang et al., 2020; Grendaitė et al., 2018; Peterson et al., 2020).

These weaknesses of monitoring water quality through in-situ point sampling can now be overcome using geospatial technologies, including remotely sensed satellite images (Zhang et al., 2020). Previously, satellite images did not have the spatial resolution needed to monitor small to medium-sized water bodies; however, advancements in remote sensing technologies have made it possible to monitor freshwater bodies remotely. For example, the release of Landsat 8 and Sentinel 2 satellites, with improved spatial resolution, radiometric resolution, and signal-to-noise ratio, has made monitoring small and medium-sized freshwater bodies possible (Grendaitė et al., 2018; Malahlela et al., 2018; Peterson et al., 2020).

Studies conducted on water quality and remote sensing have made use of algorithm development, in-situ water samples, and satellite data to monitor water quality parameters remotely (Bonansea et al., 2019; Chen et al., 2017; Karaoui et al., 2019; Mushtaq and Lala, 2017; Yepez et al., 2018; Bande et al., 2018).

This study focused on developing algorithms for monitoring chl-a and TSS in the Inanda Dam using Landsat 8 and Sentinel 2 satellite imagery.

1.2 PROJECT AIMS

The aim of this study was to develop algorithms for monitoring water quality in the Inanda Dam using Landsat 8 and Sentinel 2 satellite imagery.

1.3 OBJECTIVES

1. To develop algorithms to monitor chl-a in the Inanda Dam.
2. To develop algorithms to monitor TSS in the Inanda Dam.
3. To produce maps showing the surface distribution of chl-a in the Inanda Dam.
4. To produce maps showing the surface distribution of TSS in the Inanda Dam.

1.4 SCOPE AND LIMITATIONS

There are various water quality parameters such as Coloured Dissolved Organic Matter (CDOM), Secchi Disk Depth (SDD), Turbidity, Total Phosphorous (TP), and Total Nitrogen (TN), which can also be inferred from remote sensing. However, this study focuses on chl-a and TSS due to their abilities to reflect spectral signatures which can be recorded by remote sensors (Markogianni et al., 2017; Pu et al., 2019). This study was conducted in the Inanda Dam (Durban, KZN Province, South Africa), and fieldwork was undertaken once during the dry and wet seasons, respectively, due to budget constraints. Therefore, the algorithms developed in this study apply only to the Inanda Dam and may not yield accurate results for other dams in South Africa.

CHAPTER 2: LITERATURE REVIEW

2.1 INTRODUCTION

Water quality includes the physical, chemical, and biological parameters of a water body (Gholizadeh et al., 2016). The quality of a water body can be affected by multiple factors, such as climate change, invasive species, agricultural runoff, industrial pollution, increasing anthropogenic activities, acidification, nutrient enrichment, eutrophication, and natural factors, among many others. (Ritchie et al., 2003; Palmer et al., 2015; Ciancia et al., 2020).

Freshwater bodies, made up of lakes, dams, rivers, and groundwater, are vital to humans and the environment (Pu et al., 2019). Monitoring freshwater bodies regularly and on a large scale has become crucial to ensuring their sustainability, considering freshwater shortages and pollution (Pu et al., 2019; Bonansea et al., 2019). This literature review focuses on water quality worldwide, monitoring water quality, Landsat 8 and Sentinel 2 satellites, methodologies used to estimate chl-a and TSS remotely, and remotely sensed water quality monitoring in a South African context.

2.2 WATER QUALITY WORLDWIDE

Markogianni et al. (2017, pg 906) consider water as "essential for the survival of all living organisms." At its core, freshwater resources are a vital component of human survival and development (Li et al., 2018; Bande et al., 2018). Lakes, rivers, dams, groundwater, and reservoirs provide water for human consumption, food supplies, transportation, recreation, economic development, industries, and human health (Markogianni et al., 2017; Pirasteh et al., 2020). Freshwater bodies also help to maintain the carbon cycle, provide habitats for aquatic organisms, and ensure sustainable development, which indirectly impacts the quality of life for people (Soomets et al., 2020). Despite these numerous functions and services, freshwater resources are polluted due to anthropogenic factors such as overpopulation, industrialization, agricultural runoff, climate change, eutrophication, domestic effluent, sewerage disposal, and much more (Hu et al., 2021; Zhang et al., 2020). Pollution has led to the rapid decline of freshwater resources and their biodiversity, reduction in the supply of drinking water, contamination of aquatic food, and negative impacts on social and economic growth (Pirasteh et al., 2020). It is therefore imperative to monitor and manage available freshwater resources, through various water quality parameters (Section 2.3).

2.3 MONITORING WATER QUALITY

Monitoring freshwater is paramount to ensuring the sustainability and quality of water bodies. Many parameters can be measured in water bodies, including but not limited to chl-a, TSS, CDOM, Dissolved Organic Carbon (DOC), TP, TN, Electric Conductivity (EC), algae, phytoplankton, turbidity, and water clarity (Sharaf El Din, 2020; Guo et al., 2020; Mustaq and Lala, 2017; Bonansea et al., 2019). Traditionally, this was done using in-situ water quality monitoring, a time-consuming, labour-intensive, and expensive method. Point sampling, while very accurate, can only give the concentration of a parameter at a specific point and does not account for the spatial distribution of a water quality parameter throughout a water body (Zhang et al., 2020; Grendaitė et al., 2018; Peterson et al., 2020). It is also impossible to conduct in-situ water quality monitoring in inaccessible areas. These limitations make it difficult for water bodies to be efficiently managed. Remote sensing is now used to aid in monitoring water quality. The monitoring of small and medium-sized water bodies, which was previously a challenge, has been made possible by recent advancements in satellite technology.

For example, Landsat 8 and Sentinel 2, with their improved specifications, have been used to monitor water quality worldwide with positive results (Grendaitė et al., 2018; Malahlela et al., 2018; Peterson et al., 2020).
Water quality parameters can be broken into two main categories, namely optically active and non-optically active (Guo et al., 2020). Optically active parameters such as chl-a, TSS, CDOM, and algae affect the optical properties of water and can change the signals acquired by satellites (Markogianni et al., 2017). On the contrary, non-optically active parameters such as TP, TN, Chemical Oxygen Demand (COD), and pH have little to no optical signals and cannot influence spectral signatures of water bodies (Pu et al., 2019). Often, non-optically active parameters can be inferred indirectly by correlating optically active parameters with non-optically active parameters (Pu et al., 2019). Most studies have focussed on optically active parameters, achieving successful results. Two standard water quality parameters estimated from satellite imagery are chl-a and TSS. The monitoring of chl-a and TSS is vital for freshwater resource management as they can inform water management institutions on the quality of the water bodies they manage (Elangovan and Murali, 2019; Manuel et al., 2020; Ciancia et al., 2020).
Chl-a can be used as an indicator of the trophic status of a water body and phytoplankton activity, which is often the cause of harmful algal blooms and eutrophication (Markogianni et al., 2017; Soomets et al., 2020; Ledesma et al., 2010; Li et al., 2021a). TSS consists of solids that originate from various sources and can include among others, phytoplankton (living and dead), clay minerals, humic substances, and detritus. (Ciancia et al., 2020). TSS is often a proxy for pollutants entering a water body, and excess TSS can harm dams, affect photosynthesis and dissolved oxygen levels, and cause harmful algal blooms (Peterson et al., 2018; Soomets et al., 2020). In addition, increased discharge of sediments into water bodies causes turbidity, increasing siltation, and decreasing water quality (Yanti et al., 2016). Both chl-a and TSS can significantly influence the optical properties of a water body. With the use of satellite imagery, in-situ concentrations, and mathematical methods, chl-a and TSS can be estimated using Landsat 8 and Sentinel 2 (Sharaf El Din, 2020; Molkov et al., 2019; Bresciani et al., 2018; Ciancia et al., 2020; He et al., 2021).

2.4 LANDSAT 8 AND SENTINEL 2

Landsat 8 was launched on the 11th of February 2013 and is the eighth satellite in the Landsat series (USGS, 2021). It has a 12-bit radiometric resolution, a temporal resolution of 16 days, a spatial resolution of 30 m for bands 1 to 9, and 100 m for bands 10 and 11 (USGS, 2021). Sentinel 2 comprises two satellites, namely Sentinel 2A and Sentinel 2B, launched on the 23rd of June 2015 and the 07th of March 2017, respectively (ESA, 2021). Sentinel 2 satellites also have a 12-bit radiometric resolution, a temporal resolution of 10 days per satellite and five days when both satellites are taken into consideration, and a spatial resolution of 10 m for bands 2, 3, 4, and 8; 20 m for bands 5, 6, 7, 8a, 11 and 12; and 60 m for bands 1, 9 and 10 (ESA, 2021). In addition, Landsat 8 collects data using 11 bands, while Sentinel 2 collects data using 13 bands, and when all three satellites are used in tandem, the revisit time decreases considerably (Toming et al., 2016; Buma and Lee, 2020). The number of bands used to collect information, the temporal resolution, and improved spatial and radiometric resolutions of both Landsat 8 and Sentinel 2 makes it possible to monitor water quality in water bodies that were previously too small to be monitored using remote sensing (Yepez et al., 2018; Bande et al., 2018; Peterson et al., 2020). Table 2.1 below shows the names of each band, their spatial resolutions, and spectral wavelengths.

Table 2.1: Landsat 8 and Sentinel 2 bands, band names, spatial resolutions, and spectral wavelengths (USGS, 2021; ESA, 2021)

	Landsat 8			**Sentinel 2**		
Band Number	**Band Name**	**Spatial Resolution (m)**	**Spectral wavelength (nm)**	**Band Name**	**Spatial Resolution (m)**	**Spectral wavelength (nm)**
Band 1 (B1)	Coastal Aerosol	30	430-450	Coastal Aerosol	60	443
Band 2 (B2)	Blue	30	450-510	Blue	10	490
Band 3 (B3)	Green	30	530-590	Green	10	560
Band 4 (B4)	Red	30	640-670	Red	10	665
Band 5 (B5)	NIR	30	850-880	Vegetation Red Edge	20	705
Band 6 (B6)	SWIR 1	30	1570-1650	Vegetation Red Edge	20	740
Band 7 (B7)	SWIR 2	30	2110-2290	Vegetation Red Edge	20	783
Band 8 (B8)	Panchro matic	30	500-680	NIR	10	842
Band 8a (B8a)	-	-	-	Vegetation Red Edge	20	865
Band 9 (B9)	Cirrus	30	1360-1380	Water vapour	60	940
Band 10 (B10)	TIRS 1	100	1060-11190	SWIR – Cirrus	60	1375
Band 11 (B11)	TIRS 2	100	11500-12510	SWIR	20	1610
Band 12 (B12)	-	-	-	SWIR	20	2190

The spectral region from 400-1000 nm is often used for remotely sensed water applications; however, due to the strong absorption by water at wavelengths greater than 750 nm, wavelengths between 400-750 nm are generally used (Matthews, 2011).

Literature shows a strong absorption of chl-a in the blue and red regions of the electromagnetic spectrum, with reflectance peaks found at 550 nm and 700 nm. Many chl-a algorithms have used the reflectance peak near 700 nm and a 700 nm/670 nm colour ratio algorithm or variations for chl-a estimation (Matthews, 2011). The reflectance peak near 700 nm and the green, red, blue, and NIR regions of the electromagnetic spectrum are beneficial for chl-a estimation and inland water quality remote sensing (Gholizadeh et al., 2016).

Studies show that TSS can influence the visible (blue, green, and red) and NIR regions of the electromagnetic spectrum (Yepez et al., 2018; Gholizadeh et al., 2016). A reflectance peak at 700 nm can be used for TSS retrieval in water bodies with lower TSS concentrations (Matthews, 2011). The first four bands of Landsat are sensitive to TSS; however, one study found the spectrum range between 700 nm to 800 nm and a single band around the spectral regions of 500-900 nm helpful in TSS estimation (Gholizadeh et al., 2016).

Based on the information found in the literature, it can be inferred that Landsat 8 B1 to B5 and Sentinel 2 B1 to B8a, which fall within the spectral region of 400 nm to 900 nm, can be helpful in chl-a and TSS retrieval from satellite imagery, further discussed in Section 4.3.

2.5 METHODS EMPLOYED TO ESTIMATE WATER QUALITY PARAMETERS REMOTELY

Studies abound on the use of in-situ water samples, satellite data, and mathematical methods for the estimation of water quality parameters remotely (Bonansea et al., 2019; Chen et al., 2017; Karaoui et al., 2019; Mushtaq and Lala, 2017; Yepez et al., 2018; Bande et al., 2018). Mathematical methods consist of analytical and statistical/empirical methods used to develop algorithms for monitoring water quality parameters; however, both methods have pros and cons. For example, statistical methods are easier to understand and implement.

However, the algorithms developed are site and time-specific and do not account for any significant variations in the water body. On the contrary, analytical methods are more complex to understand, develop and implement; however, the algorithms generated can generally be used for many water bodies and at any time of the year (Gholizadeh et al., 2016).

Studies related to the retrieval of water quality parameters from satellite imagery requires a generic number of steps (Matthews, 2011) summarized as follows:

- Pre-processing of satellite imagery
- Correlation of bands/band ratios with in-situ water quality parameters
- Algorithm development

2.5.1 Pre-processing

Remotely sensed imagery often contains flaws or deficiencies which need to be rectified before use for an application; hence the correction of these flaws is done before any information is extracted from the imagery, a process termed pre-processing (Mather and Koch, 2011). There are many types of image correction methods applied to a variety of distortions, and this can be grouped into generic headings, namely atmospheric and radiometric corrections (Lillesand et al., 2000).

2.5.1.1 Atmospheric correction

An atmospheric correction needs to be performed on satellite imagery to remove atmospheric effects, which may cause errors in a study (Pu et al., 2019). Many atmospheric correction methods have been used in different studies. While there is no agreement on the best method to be used, there is a consensus that atmospheric corrections must be performed before analysis (Olmanson et al., 2020; Ansper and Alikas, 2019). Table 2.2 below lists the atmospheric correction methods used in Landsat 8 and Sentinel 2 imagery pre-processing.

Table 2.2: Atmospheric correction methods used on Landsat 8 and Sentinel 2 imagery (Source: author's work)

Atmospheric correction method	Satellite used	Study
Dark Object Subtraction (DOS)	Landsat 8	Markogianni et al., 2017; Boucher et al., 2018; Masocha et al., 2018; Gonzalez-Marquez et al., 2018; Sharaf El Din and Zhang, 2017.
Landsat-8 surface reflectance code (LaSRC)	Landsat 8	Rodrigues et al., 2017; Chen et al., 2019; Prasad et al., 2020; Peterson et al., 2020; Yepez et al., 2018; Pham et al., 2018; Vinh et al., 2019.
Second Simulation of Satellite Signal in the Solar Spectrum (6S)	Landsat 8 and Sentinel 2	Bresciani et al., 2018; Li et al., 2017; Zhu et al., 2019; Li et al., 2018; Bonansea et al., 2019; Cairo et al., 2020; Laili et al., 2015; Giardino et al., 2014; Zhang et al., 2016.
Fast Line-of-sight Atmospheric Analysis of Hypercubes (FLAASH)	Landsat 8 and Sentinel 2	Yadav et al., 2019; Pu et al., 2019; Kurniadin and Jaelani, 2016; Buma and Lee, 2020; Larson et al., 2021; Ansari and Akhoondzadeh, 2020; Quang et al., 2017; Bande et al., 2018; Fadel et al., 2016; Alcantara et al., 2016; Chen et al., 2017; Watanabe et al., 2015; Rodrigues et al., 2017; Kutser et al., 2016.

Atmospheric correction method	Satellite used	Study
Quick atmospheric correction (QAC)	Landsat 8	Malahlela et al., 2018; Yang and Anderson, 2016; Kutser et al., 2016.
Model-based empirical line method (MoB-ELM)	Landsat 8 and Sentinel 2	Concha and Schott, 2016; Ha et al., 2017
The Management Unit of the North Seas Mathematical Models (MUMM)	Landsat 8 and Sentinel 2	Wang et al., 2021
ACOLITE	Landsat 8 and Sentinel 2	Molkov et al., 2019; Rodrigues et al., 2017.
Sen2Cor	Sentinel 2	Guo et al., 2021; Shang et al., 2021; Ouma et al., 2020; Grendaitė et al., 2018; Sòria-Perpinyà et al., 2020; Peterson et al., 2020; Huangfu et al., 2020; Li et al., 2021b; Al-Kharusi et al., 2020; Bande et al., 2018; Lui et al., 2017.
Case 2 Regional Coast Colour (CR2CC)	Sentinel 2	Li et al., 2021a; Ansper and Alikas, 2019; Hassan et al., 2021.
POLYMER	Sentinel 2	Aptoula and Ariman, 2021
ATCOR23	Landsat 8	Kutser et al., 2016; Rodrigues et al., 2017.
Dark Pixel (DP) method MIP	Landsat 8 Sentinel 2	Patra et al., 2017; Kutser et al., 2016; Dornhofer et al., 2016.

In relation to the many atmospheric correction methods employed in various studies (Table 2.2), FLAASH is the favoured atmospheric correction method for Landsat 8 images, and Sen2Cor has been used extensively for Sentinel 2 images. Studies have, however, indicated that no one atmospheric correction method outperformed the other, and there is still much disagreement as to the best atmospheric correction method for water quality studies (Molkov et al., 2019; Ansper and Alikas, 2019).

2.5.1.2 Radiometric Correction

Radiometric correction is performed on imagery to convert Digital Numbers (DN) to radiance or reflectance. For example, Landsat 8 DN are often converted to radiance and reflectance values using metadata files (Markogianni et al., 2017; Bonansea et al., 2019; Ouma et al., 2020; Yadav et al., 2019; Malahlela et al., 2018; Pu et al., 2019; Peterson et al., 2018; Buma and Lee, 2020; Boucher et al., 2018; Ansari and Akhoondzadeh, 2020; Mushtaq and Lala, 2017; Masocha et al., 2018; Li et al., 2018); however, Hydrolight was used by Chen et al. (2019), and DOS by Elangovan and Murali (2020) to obtain remote sensing reflectance.

Sentinel 2 imagery is already radiometrically corrected (ESA, 2021); therefore, no radiometric corrections are needed; however, these imageries come in three resolutions and must be resampled to a standard resolution (Sòria-Perpinyà et al., 2020). Resampling to a standard resolution can be done using the Resampling function in SNAP software (Ansper and Alikas, 2019).

2.5.2 Band correlations

Landsat 8 and Sentinel 2 bands are often correlated with in-situ water quality parameters to determine which band/band ratios can estimate a specific water quality parameter. The use of band combinations, rather than single bands, often produces better correlation results with in-situ water quality parameters, achieving better water quality parameter estimations (Kim et al., 2016; Masocha et al., 2018).

Studies conducted have made use of Landsat 8 B1 to B7 (Prasad et al., 2020; Ledesma et al., 2019) and all Sentinel 2 bands, either in the form of single bands or band ratios to determine chl-a and TSS; however, results are varied across the studies, with an indication that band ratios perform better than single bands at estimating chl-a and TSS (Sharaf El Din, 2020; Kim et al., 2016; Masocha et al., 2018).

2.5.3 Algorithm development

Many algorithms can be used to estimate water quality parameters from satellite imagery. However, empirical/statistical methods are easier to understand and are the most used algorithm development method. For example, regression analysis is a common statistical method that is performed to generate algorithms to estimate water quality parameters (Markogianni et al., 2017; Ledesma et al., 2019; Ouma et al., 2020; Li et al., 2021b; Grendaitė et al., 2018; Malahlela et al., 2018; Deutsch et al., 2014; Kurniadin and Jaelani, 2016; Kontopoulou et al., 2017; Yang and Anderson, 2016; Elangovan and Murali, 2020; Karaoui et al., 2019, Mushtaq and Lala, 2017; Yepez et al., 2018; Fadel et al., 2016; Patra et al., 2017; Kim et al., 2016; Lim and Choi, 2015; Masocha et al., 2018; Liu et al., 2017; Sharaf El Din and Zhang, 2017; Lailia et al., 2015; Ha et al., 2017; Al-Fahdawi et al., 2015). Physically-based methods are more complex and require an in-depth understanding of Inherent Optical Properties (IOP) and are less frequently used (Bresciani et al., 2018; Manuel et al., 2020; Zhang et al., 2016; Giardino et al., 2014; Manzo et al., 2015; Dornhofer et al., 2016). In recent years, there has been much development in the field of machine learning and Artificial Neural Networks (ANN), with promising results (Prasad et al., 2020; Peterson et al., 2020; Peterson et al., 2018; Larson et al., 2021), allowing for the exploration of more research in this area of algorithm development.

Despite the simplicity of empirical methods, they have been able to estimate both chl-a and TSS from Landsat 8 and Sentinel 2 with varying levels of accuracy. Most studies did obtain good correlations with chl-a and TSS (R^2 = 0.7 and more), while fewer studies achieved less successful correlations (R^2 = 0.5 and less). The physically-based methods vary from successful to limited, indicating that more research must be done in this area of water quality and remote sensing. ANN and machine learning have outperformed empirical methods in comparative studies (Prasad et al., 2020; Pu et al.), indicating the possibilities of these methods in water quality estimation from satellite imagery.
There are many methods available to retrieve water quality parameters from satellite imagery. Each method has its pros and cons; however, the simplicity of empirical models coupled with the positive results emanating from its use makes them the most popular method to use (Matthews, 2011).

2.6 SOUTH AFRICAN CONTEXT

South Africa is a water-scarce country, with dams dropping to low levels and rivers having low flows occasionally (Donnenfeld et al., 2018). Overexploitation of water resources will cause ecosystems to deteriorate and water quality to decline. This can adversely impact South Africa by causing water-borne diseases and hindering social and economic development (Donnenfeld et al., 2018). Due to increasing population in South African and the resulting increase in the demand for water supply (Donnenfeld et al., 2018), the management of water resources to meet these demands is now crucial, and remote sensing can be used as a cost-effective tool in managing the water quality of South Africa's various freshwater resources.
Internationally, many studies were conducted to monitor water quality using remote sensing (Ledesma et al., 2019; Ouma et al., 2020; Li et al., 2021a; Grendaitė et al., 2018; Deutsch et al., 2014; Bresciani et al., 2018; Manuel et al., 2020; Zhang et al., 2016; Giardino et al., 2014; Manzo et al., 2015;), however the studies conducted in South Africa are limited. For example, Matthews (2014) looked at eutrophication by monitoring chl-a, cyanobacteria, and surface scum with the use of Medium Resolution Imaging Spectrometer (MERIS) and water quality algorithms, and Malahlela et al. (2018) and Bande et al. (2018) estimated chl-a and turbidity using Landsat 8 and Sentinel 2 imagery with fair accuracy. In their study, Bande et al. (2018) found that Sentinel 2 estimated chl-a and turbidity better than Landsat 8. Studies conducted in South Africa, while

successful, are limited, leaving a research gap in the field of remotely sensed water quality to be filled. More studies conducted in remote sensing and water quality will develop the potential for large scale monitoring of freshwater resources using satellite imagery in South Africa.

CHAPTER 3: METHODOLOGY

3.1 STUDY AREA

The Inanda Dam is located in Kwangcolosi, Valley of a Thousand Hills, 42 km from Durban and 24 km from Hillcrest, in KZN Province, South Africa (Figure 3.1). The depth, length, and surface area of the Dam are estimated to be 50 m, 23 km, and 14400000 m^2, with a total capacity of 256000000 m^3 (Agunbiade and Moodley, 2014). The coordinates of its inlet and outlet are at 29°39′05.20″S, 30°48′06.24″E and 29°42′55.74″S, 30°52′07.69″E, with its wall located at 29°42'38.88" S, 30°52'12"E (Agunbiade and Moodley, 2014). The Dam is one of four dams found on the uMngeni River, which on a larger scale forms part of the uMngeni catchment, with the uMngeni river flowing from the foothills of the Drakensburg Mountains into the Indian Ocean in the coastal city of Durban (Namugize et al., 2018; Agunbiade and Moodley, 2014; Matongo et al., 2015; Tinmouth, 2009). The climate of this study area is subtropical, characterized by dry winters and wet summers, with most of the rainfall received during the summer months of October to March (Ngetar, 2002; Namugize et al., 2018). While the average rainfall of this region is between 900-1000 mm (Ngetar, 2002), Manickum (2020) found that the average rainfall over the Inanda Dam between the years 2017-2019 was 644.7 mm. The surrounding area of the Dam is characterized by hilly, undulating landscapes and agricultural activities practised by the surrounding rural communities (Nkoana, 2014; Rangeti, 2014). The Inanda Dam is a vital source of drinking water for the surrounding areas (Fischer et al., 2019).

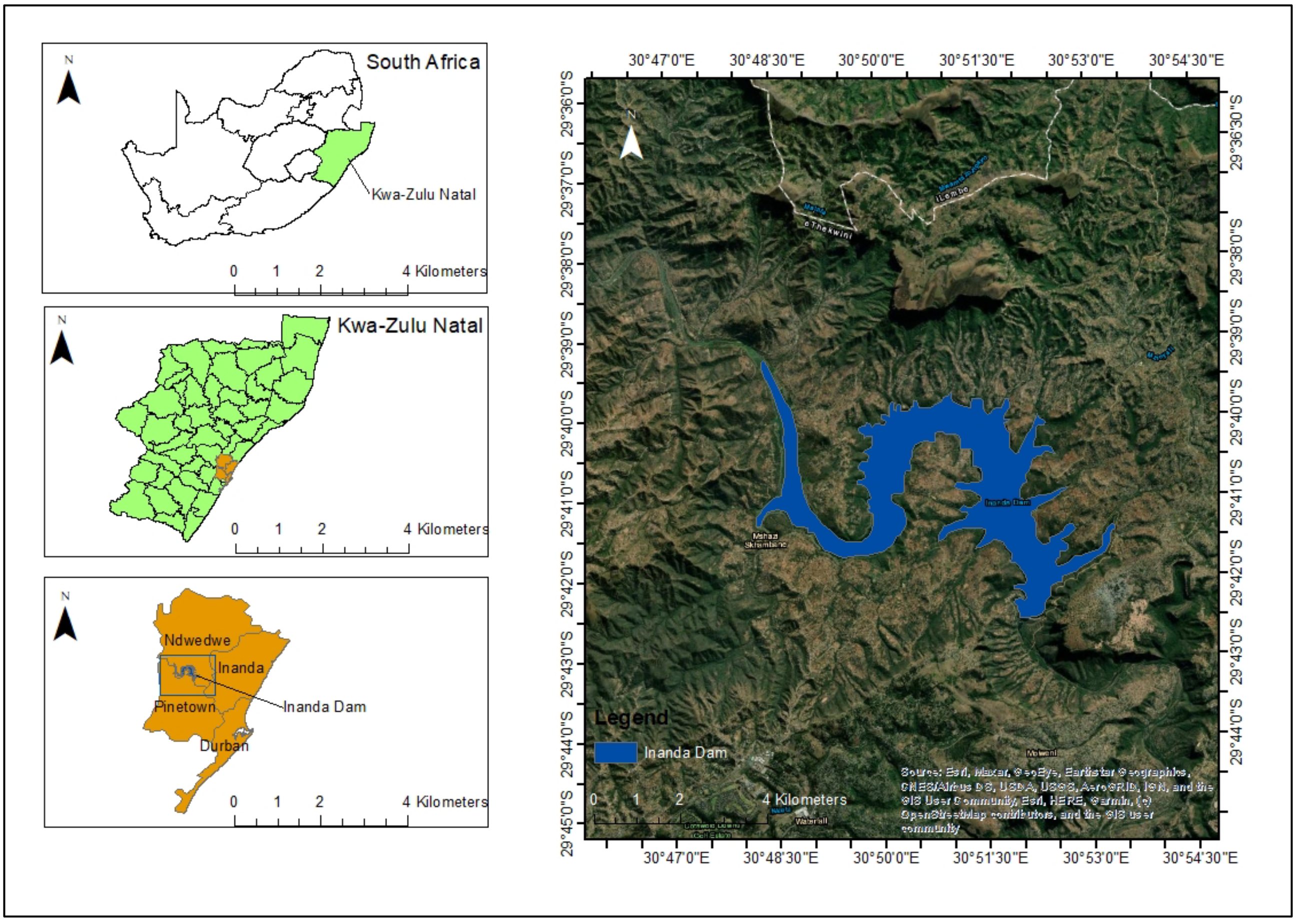

Figure 3.1: Map of Inanda Dam and its surrounding locations in KwaZulu-Natal, South Africa.

3.2 FIELDWORK

Water samples were collected during different seasons to account for the seasonal differences in water quality. The wet and dry season in-situ water samples were collected from the Inanda Dam on the 06th of March 2020 and the 12th of May 2021, respectively. In-situ sampling days were chosen to closely coincide with Landsat 8 satellite overpass, which occurred on the 07th of March 2020 (wet season) and the 12th of May 2021 (dry season), while the Sentinel 2 overpass was on the 04th of March 2020 (wet season) and the 13th of May 2021 (dry season) (Figure 3.1). Forty-five water samples were collected randomly in the Inanda Dam on both sampling dates. Two water samples were collected at each sampling point to test for chl-a and TSS. The GPS coordinates of each sample were also recorded. Nine samples could not be used from the two sets of 45 samples due to errors in the data. The remaining 81 samples (Figure 3.2) were split into 70% or 57 samples to develop the algorithms and 30% or 24 samples to validate the developed algorithms.

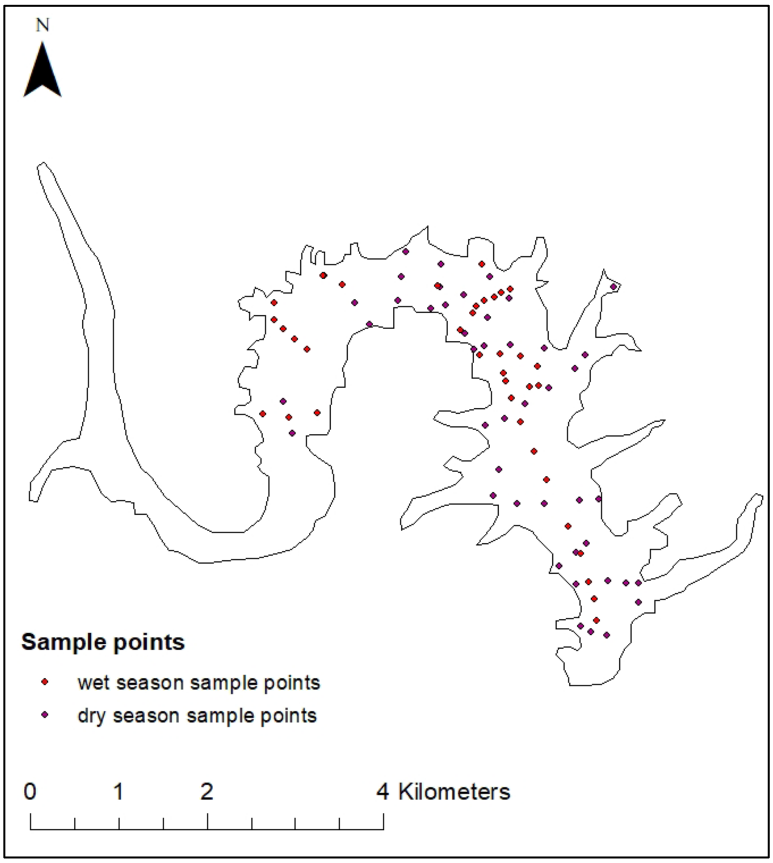

Figure 3.2: Location of wet and dry season sampling points in the Inanda Dam.

3.3 LABORATORY ANALYSIS

3.3.1 TSS

TSS concentration was determined using the filtration method described in the Standard Methods for the Examination of Water and Wastewater (Sharaf El Din, 2020) and included the quantitative filtration of a sample test portion through a glass fibre filter. Gravimetric determination of the retained residue on the filter was gauged after drying at 105 ± 2°C. This method was favoured for its use in numerous studies (Sharaf El Din, 2020; Soomets et al., 2020; Yanti et al., 2016; Molkov et al., 2019).

3.3.2 Chl-a

Chl-a concentration was determined using spectrophotometry, a method promoted in various studies due to its accuracy (Prasad et al., 2020; Soomets et al., 2020; Ledesma et al., 2019; Zhang et al., 2020; Li et al., 2021a; Ansper and Alikas, 2019; Molkov et al., 2019; Elangovan and Murali, 2020). The actual procedure is described in Standard Methods for the Examination of Water and Wastewater (Prasad et al., 2020). It consists of filtering water samples to concentrate the organisms which contain chl-a. Next, the cells were ruptured, and the chl-a was extracted using organic solvent acetone. The extract was then analysed via a spectrophotometric method using the known optical properties of chl-a.

3.4 PRE-PREPROCESSING OF SATELLITE IMAGERY

Landsat 8 satellite images were downloaded from the United States Geological Survey (USGS) website and Sentinel 2 images from the European Space Agency (ESA) Copernicus Hub. Landsat 8 images were radiometrically pre-processed to obtain the radiance and reflectance values for B1 to B7. Radiance values for the Landsat 8 images were obtained from ENVI 5.2. using the following formula:

$L_\lambda = M_L Q_{cal} + A_L$, where:

- L_λ = TOA spectral radiance (Watts/(m^2 * srad * μm))
- M_L =Band-specific multiplicative rescaling factor from the metadata (RADIANCE_MULT_BAND_x, where x is the band number)
- Q_{cal} = Quantized and calibrated standard product pixel values (DN)
- A_L=Band-specific additive rescaling factor from the metadata (RADIANCE_ADD_BAND_x, where x is the band number)

Reflectance values for each pixel were obtained using the FLAASH Atmospheric correction module found on ENVI 5.2. software, which converted the DN of each pixel into reflectance values for each pixel. The use of reflectance instead of radiance values in remote sensing analysis has been favoured because reflectance is a property of the target material itself and will give the most accurate results (L3Harris Geospatial, 2013). The radiance and reflectance values were extracted from bands 1 to 7 of the Landsat 8 images for the 81 GPS sampled points used in algorithm calibration and validation. The radiance and reflectance data for band ratios were calculated using simple mathematical formulas in Microsoft Excel for example:

$Radiance/Reflectance = \frac{B2}{B1}$, where:

B2 is the radiance of Landsat 8 B2
B3 is the radiance of Landsat 8 B3

Sentinel 2 images can be downloaded in two formats, Top-of-Atmosphere (TOA) reflectance and Bottom-of-Atmosphere (BOA) reflectance. TOA reflectance images need to be resampled so that all bands have the same spatial resolution (Sòria-Perpinyà et al., 2020), and this was done using the resampling function in SNAP

(Ansper and Alikas, 2019). The BOA reflectance images are already atmospherically corrected and resampled to one spatial resolution, and therefore, no pre-processing was performed on this imagery.
TOA and BOA reflectance were extracted for all 13 bands of Sentinel 2 imagery for the 81 sample points using SNAP. After that, the TOA and BOA reflectance data from each band was used to calculate the TOA and BOA reflectance for Sentinel 2 band ratios using Microsoft Excel, as was done for Landsat 8 band ratios.

3.5 BAND/BAND RATIOS AND CORRELATIONS WITH CHL-A AND TSS

The Pearson correlation was used to determine the relationship between band/band ratio radiance, reflectance, TOA, and BOA values, with in-situ chl-a and TSS. The use of a Pearson correlation was preferred as it is used to determine the relationship between two variables, in this case, satellite radiance/ reflectance and in-situ water quality concentrations, as opposed to the strength of the dependence between two variables (Kendall rank correlation) or the degree of association between two variables (Spearman rank correlation) (Statistic Solutions, 2021). This was done to determine which bands/band ratios are most sensitive for the retrieval of chl-a and TSS.

3.6 ALGORITHM DEVELOPMENT

Linear regression algorithms for monitoring chl-a and TSS in the Inanda Dam were produced in SPSS. The radiance and reflectance data obtained from Landsat 8 imagery, TOA and BOA reflectance data obtained from Sentinel 2 imagery, and in-situ chl-a and TSS concentrations for the 57 data points used to develop the algorithms were input into SPSS to develop the algorithms. Only the bands or band ratios correlating with chl-a and TSS and retaining a correlation value of 0.8 and above were used to generate the algorithms. The algorithms were generated using linear regression analysis, in the form $y = a+bx$, where a and b are statistically generated values, x represents the band/band ratios value, and y represents the estimated water quality parameter. The five most successful algorithms generated using Landsat 8 radiance, Landsat 8 reflectance, Sentinel 2 TOA, and Sentinel 2 BOA reflectance data for chl-a and TSS were validated using the remaining 24 samples to obtain the most accurate retrieval algorithms.

3.7 SURFACE DISTRIBUTION MAPS

Microsoft Excel was used to create a table including the X and Y coordinates of sample points, their corresponding in-situ chl-a and TSS concentrations, and the estimated chl-a and TSS values generated by the most successful algorithms.
ArcMap software (Version 10.8.1) was used to produce maps showing the surface distribution of chl-a and TSS in the Inada Dam. To accomplish this, the table created in Excel was imported to ArcMap to display and visualize their locations; thereafter, the software's geostatistical analysis tool and the kriging function was used to produce the surface distribution maps. Exploratory spatial data analysis tools were also used to transform the data to obtain more accurate surface distribution results. The resulting maps are continuous surface maps showing the spatial distribution of chl-a and TSS in the Inanda Dam.

CHAPTER 4: RESULTS AND DISCUSSION

4.1 INTRODUCTION

Chapter four presents the results and discusses the findings of this study. This chapter is split into four sections: in-situ water quality concentrations, correlations, algorithms, and surface distribution of chl-a and TSS over Inanda Dam. The section on in-situ water quality concentrations contains the chl-a and TSS concentrations found in the Dam during the fieldwork. The in-situ chl-a and TSS for the wet and dry seasons were determined after the two sample sessions, and their concentrations were further combined to give an overview of the seasonal concentrations in the Dam. Another reason for merging the two datasets was to improve the accuracy of results considering that the dry season data did not provide accurate correlations and algorithms for chl-a and TSS estimation. The results, presented in Sections 4.2, 4.3, 4.4, and 4.5 describes and discusses the results of the merged wet season and dry season data.

4.2 IN-SITU WATER QUALITY CONCENTRATIONS

Section 4.2 presents the results and discusses the in-situ chl-a and TSS concentrations in the Inanda Dam during the wet and dry seasons and the combined in-situ chl-a and TSS concentrations for both seasons.

4.2.1 In-situ chl-a

The in-situ spatial distribution of chl-a in the Inanda Dam on the 06th of March 2020 (Figure 4.1) and the 12th of May 2021 (Figure 4.2) shows its variation in the wet and dry seasons. Figure 4.3. displays the combined dry and wet season in-situ chl-a distribution in the Dam.

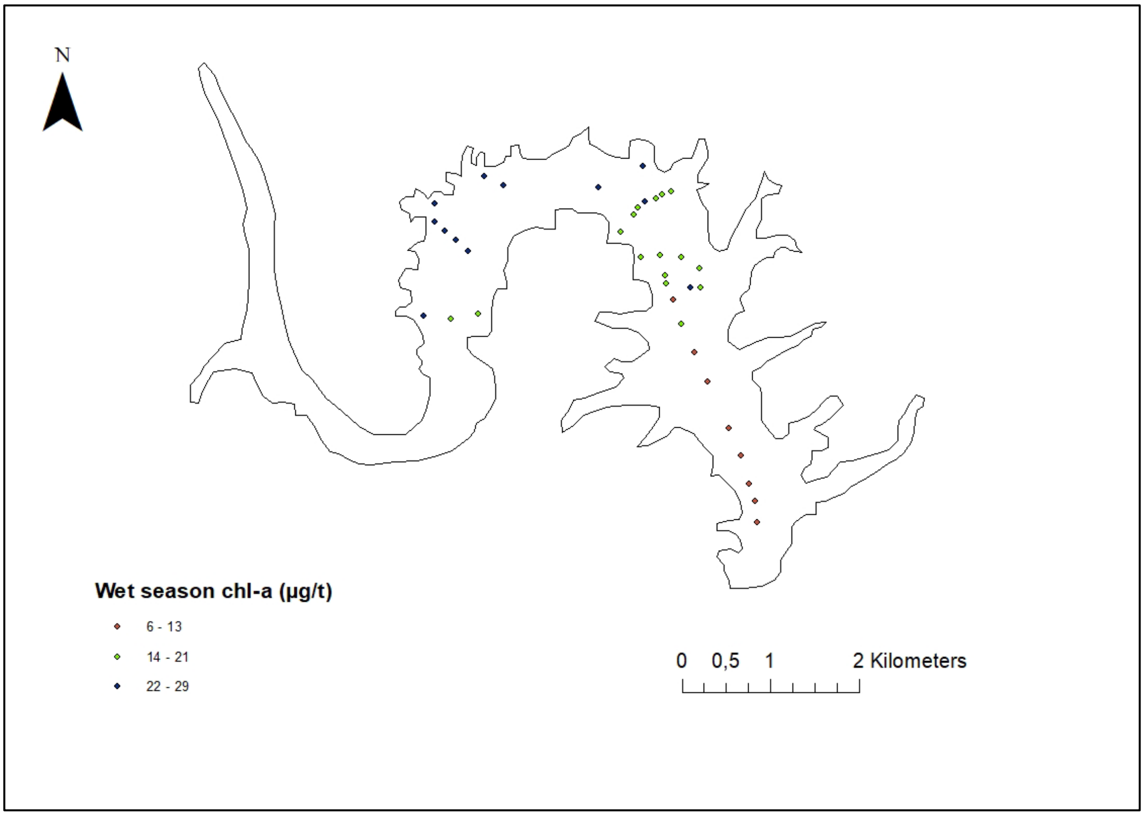

Figure 4.1: Distribution of in-situ chl-a for the wet season

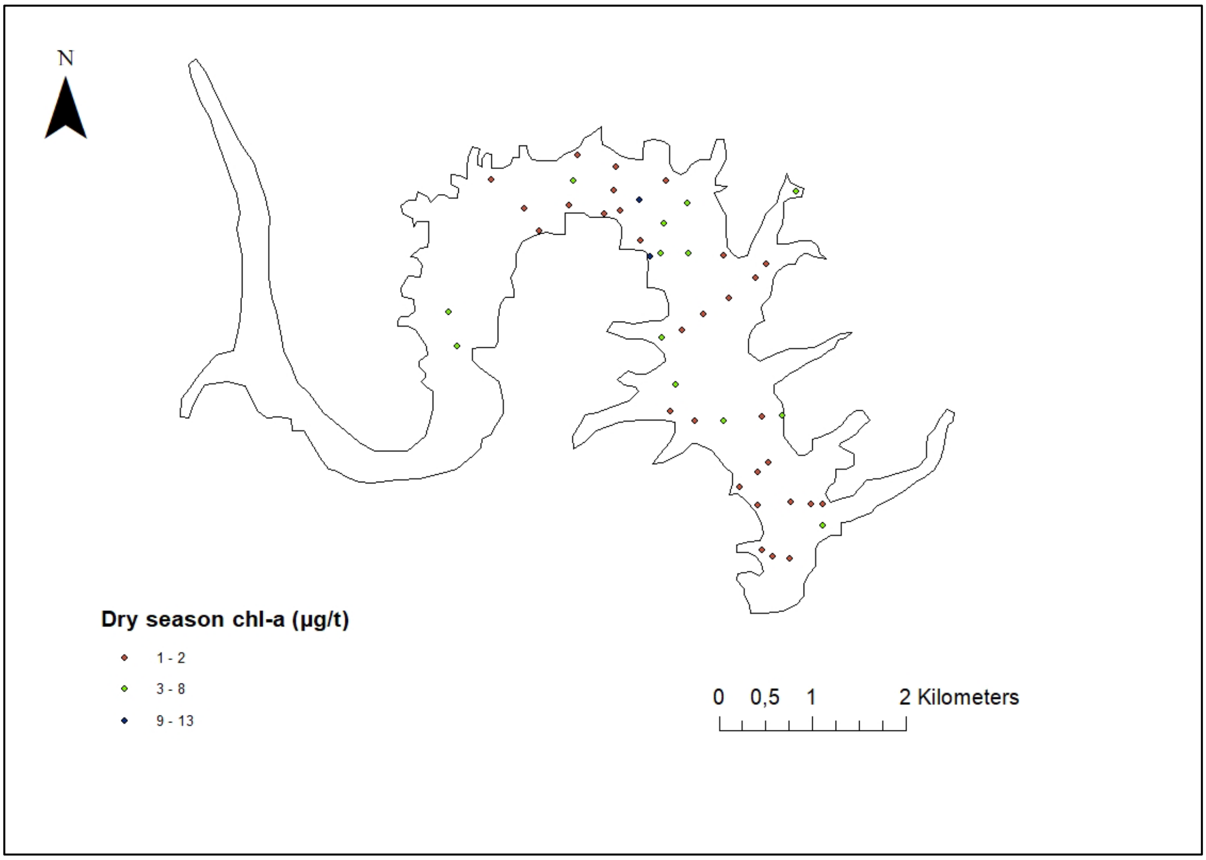

Figure 4.2: Distribution of in-situ chl-a for the dry season

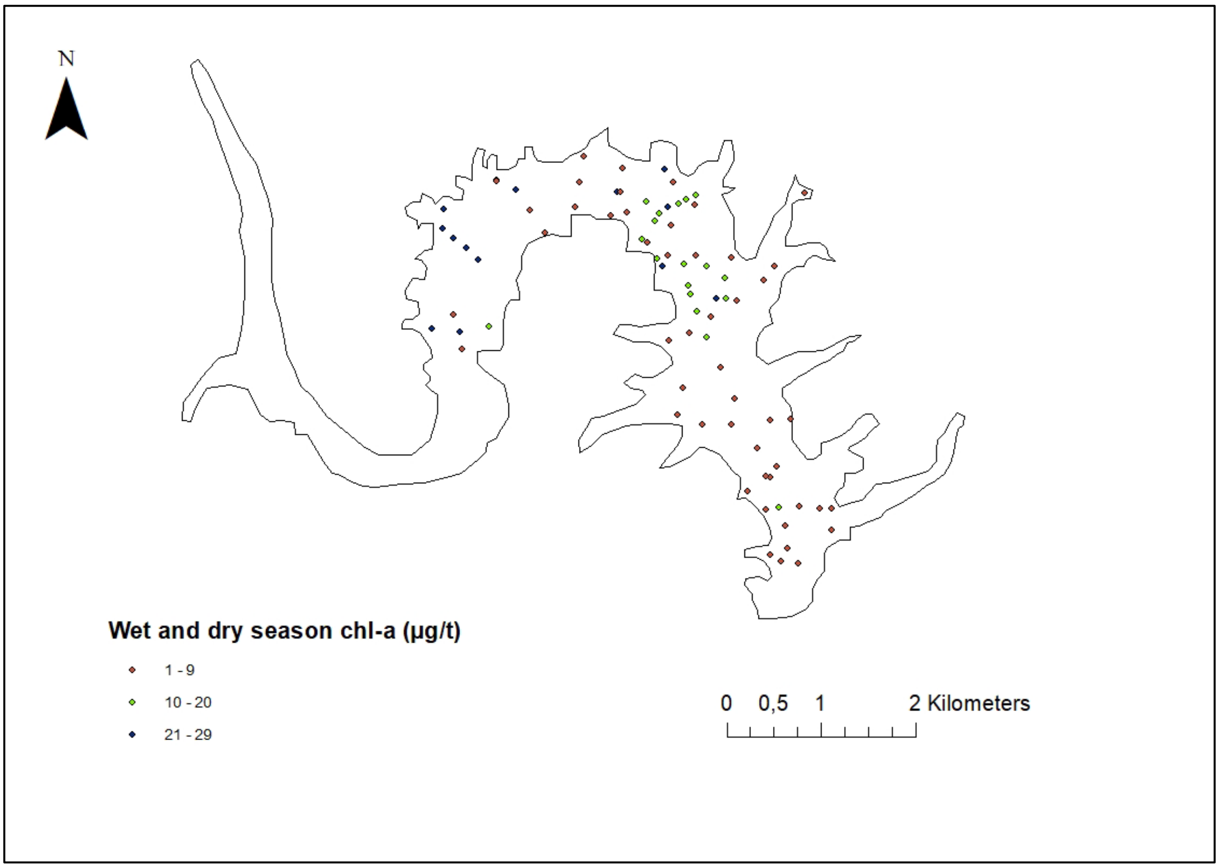

Figure 4.3: Distribution of in-situ chl-a for the wet and dry season

The wet season generally had high chl-a concentrations with a larger range (5.7µg/t to 29µg/t) (Figure 4.1), while the dry season had lower chl-a concentrations with a smaller range (0.6µg/t to 5.7µg/t) (Figure 4.2). The difference in seasonal chl-a concentrations could be attributed to different climatic conditions in the study area during the dry and wet seasons. KZN experiences high amounts of rainfall during the wet season (900-1000 mm) and high temperatures, which aid in developing chl-a (Matthews and Bernard, 2014; Ngetar, 2002; Namugize et al., 2018). The dry season experiences less rainfall and cooler temperatures, hence lower chl-a levels.

In the wet season, higher chl-a concentrations (20µg/t to 29µg/t) occur near the dam inlet, decreasing as water flows closer to the dam outlet (dam wall). This chl-a distribution pattern could be attributed to many factors, namely the meandering nature of the Dam and pollution from Darvill Wastewater Works, which releases high amounts of soluble phosphorous into the catchment (Rangeti, 2014). In addition, anthropogenic activities from Pietermaritzburg and the surrounding rural areas release pollutants into the catchment and the prevailing easterly wind direction keeps phosphorous trapped upstream, which contributes to algal production (Graham, 2004; Simpson and Pillay, 2000). The distribution of chl-a varied during the dry season, with no specific concentration pattern in the Dam (Figure 4.2).

When combined, the wet and dry season sampling results yielded chl-a ranging from 0.6µg/t to 29µg/t (Figure 4.3), indicating a high seasonal variation of chl-a in the Inanda dam, with higher chl-a concentrations in the wet season and lower chl-a concentrations in the dry season.

More research can be conducted on the role of atmospheric effects and dam circulation in the production of chl-a in the Inanda Dam.

4.2.2 In-situ TSS

The in-situ distribution of TSS in the Inanda Dam on the 06th of March 2020 (Figure 4.4) and the 12th of May 2021 (Figure 4.5) shows its variation and spatial distribution in the wet and dry seasons. Figure 4.6 displays the combined variation of the dry and wet season in-situ TSS concentrations in the Dam.

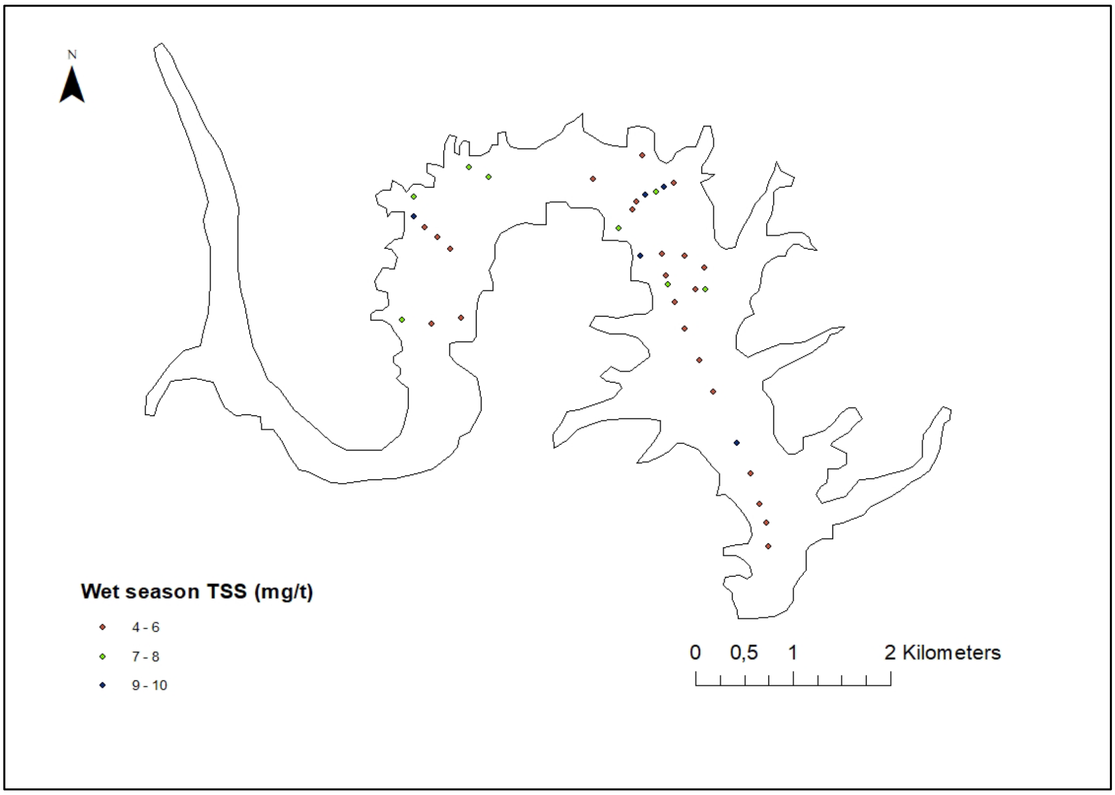

Figure 4.4: Distribution of in-situ TSS for the wet season

Figure 4.5: Distribution of in-situ TSS for the dry season

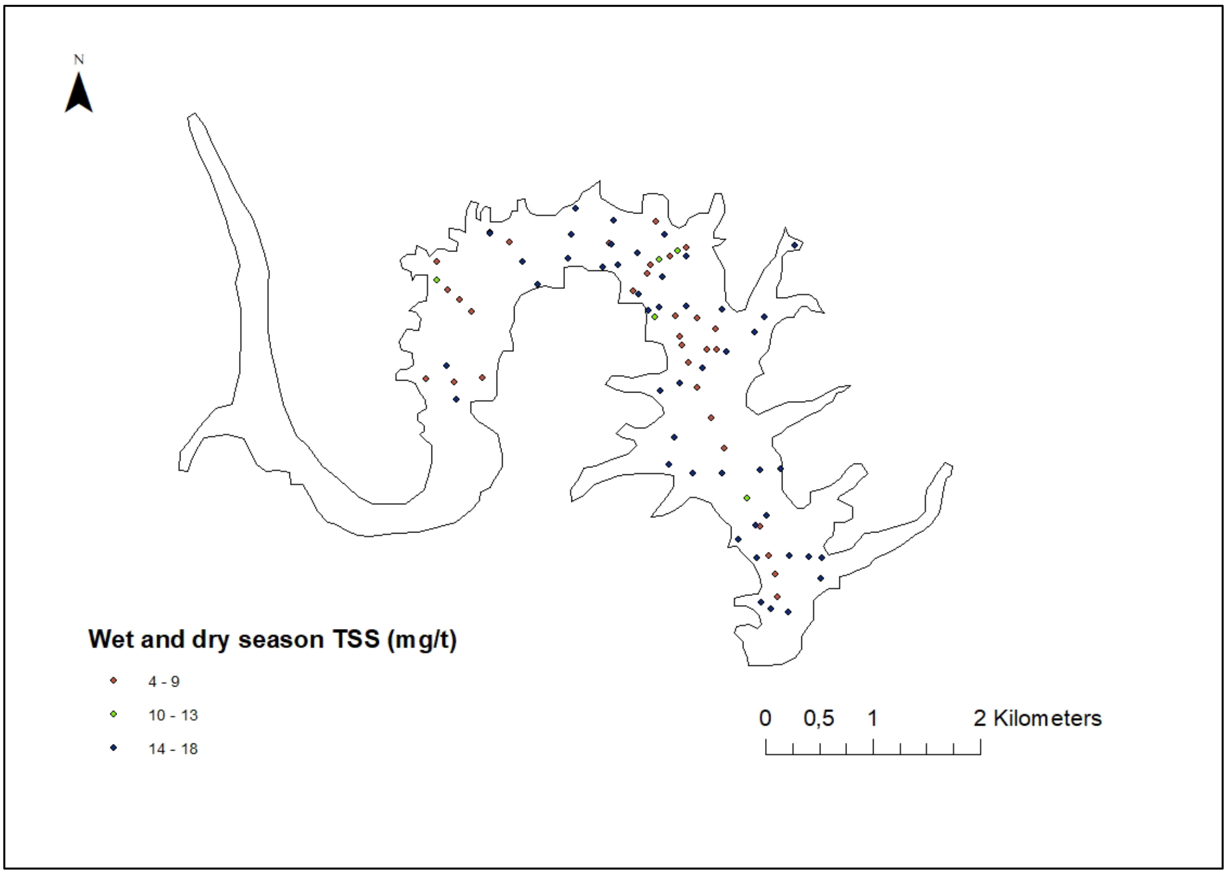

Figure 4.6: Distribution of in-situ TSS for the wet and dry season

In-situ TSS measurements indicate that there is a variation in concentrations between the wet and dry seasons. Figure 4.4 shows that the wet season had lower TSS concentrations but a larger range in concentrations (4 mg/t to 10 mg/t). The dry season had higher TSS concentrations but a small range (17.7 mg/t to 18 mg/t). Pollution from industrial areas, agriculture, and increased rainfall can lead to increases in TSS. Sharaf El Din (2020) found the highest TSS concentrations in the wet season, which decreased during the dry season, possibly due to temperature changes, pH changes, and compounds found in the water. Contrary to Sharaf El Din (2020), Ngabirano et al. (2016) in their study found high TSS levels in the dry season and low levels during the wet season, corroborating the results of this study (Figure 4.5 and Figure 4.4 respectively). The apparent disagreements emanating from these studies provides an opportunity for further research to be conducted to determine the cause of seasonal variations of TSS. Overall, the combined TSS concentrations for the two seasons ranged from 4 mg/t to 18 mg/t, with a high variation of TSS distribution over the Dam (Figure 4.6).

4.3 CORRELATIONS

4.3.1 Landsat 8

Table 4.1 displays the Pearson correlation (R-value) results between Landsat 8 radiance/reflectance and in-situ chl-a and TSS. The values highlighted in bold indicate correlations of 0.8 and higher.

Table 4.1: Correlations between Landsat 8 band/band ratio radiance and reflectance data, and in-situ chl-a and TSS

	Radiance		**Reflectance**	
Band/Band Ratio	**Chl-a**	**TSS**	**Chl-a**	**TSS**
B1	**0.862**	**-0.977**	**-0.835**	**0.983**
B2	**0.882**	**-0.970**	**-0.822**	**0.983**
B3	**0.907**	**-0.947**	0.140	0.309
B4	**0.922**	**-0.928**	-0.170	0.607
B5	**0.848**	**-0.806**	-0.598	0.768
B6	0.270	-0.239	-0.280	0.363
B7	0.227	-0.210	-0.116	0.198
B2:B1	**0.902**	**-0.910**	**0.901**	**-0.886**
B3:B1	**0.917**	**-0.927**	**0.900**	**-0.952**
B4:B1	**0.931**	**-0.886**	**0.917**	**-0.935**
B5:B1	0.572	-0.388	0.782	-0.789
B6:B1	0.019	0.033	0.763	**-0.841**
B7:B1	0.011	0.030	0.794	**-0.912**
B1:B2	**-0.900**	**0.914**	**-0.906**	**0.902**
B3:B2	**0.917**	**-0.933**	**0.889**	**-0.965**
B4:B2	**0.932**	**-0.882**	**0.912**	**-0.949**
B5:B2	0.313	-0.097	0.706	-0.734
B6:B2	-0.048	0.097	0.690	-0.797
B7:B2	-0.046	0.084	0.740	**-0.888**
B1:B3	**-0.906**	**0.949**	**-0.871**	**0.975**
B2:B3	**-0.907**	**0.950**	**-0.867**	**0.977**
B4:B3	-0.494	0.796	-0.612	**0.900**
B5:B3	-0.771	**0.907**	-0.666	0.749
B6:B3	-0.299	0.347	-0.319	0.289
B7:B3	-0.260	0.302	-0.157	0.049
B1:B4	**-0.923**	**0.917**	**-0.883**	**0.970**
B2:B4	**-0.926**	**0.908**	**-0.881**	**0.972**
B3:B4	0.491	**-0.803**	0.588	**-0.888**
B5:B4	-0.795	**0.889**	-0.654	0.701
B6:B4	-0.300	0.335	-0.250	0.167
B7:B4	-0.257	0.287	-0.031	-0.149
B1:B5	-0.576	0.391	**-0.815**	**0.885**
B2:B5	-0.265	0.038	-0.771	**0.847**
B3:B5	0.752	**-0.893**	0.772	**-0.885**
B4:B5	0.783	**-0.876**	0.793	**-0.854**
B6:B5	-0.107	0.119	0.602	**-0.808**
B7:B5	-0.084	0.092	0.617	**-0.815**
B1:B6	-0.225	0.141	-0.771	**0.895**

	Radiance		Reflectance	
B2:B6	-0.036	-0.060	-0.745	**0.878**
B3:B6	0.650	-0.750	0.521	-0.499
B4:B6	0.641	-0.699	0.378	-0.261
B5:B6	0.129	-0.110	-0.635	**0.822**
B7:B6	0.096	-0.107	0.502	-0.609
B1:B7	-0.282	0.194	-0.786	**0.898**
B2:B7	-0.105	0.006	-0.767	**0.885**
B3:B7	0.602	-0.699	0.126	-0.042
B4:B7	0.578	-0.632	-0.059	0.215
B5:B7	0.060	-0.045	-0.678	0.831
B6:B7	-0.069	0.077	-0.488	0.571

4.3.1.1. Correlation between Landsat 8 radiance/reflectance and in-situ chl-a

Landsat 8 bands B1 to B5 and band ratios B2:B1, B3:B1, B4:B1, B1:B2, B3:B2, B4:B2, B1:B3, B2:B3, B1:B4, and B2:B4 radiance, and Landsat 8 reflectance values from bands B1, B2, and band ratios B2:B1, B3:B1, B3:B2, B1:B2, B1:B3, B2:B3, B1:B4, B2:B4, B4:B1, and B4:B2 obtained correlations of 0.8 and more with in-situ chl-a. These results corroborates with the results of similar studies which also found Landsat 8 B1 to B5 to be the most sensitive in chl-a retrieval (Fadel et al., 2016; Lim and Choi, 2015; Laili et al., 2015; Watanabe et al., 2015; Al-Fahdawi et al., 2015; Patra et al., 2017; Prasad et al., 2020; Malahlela et al., 2018; Yang and Anderson, 2016; Elangovan and Murali, 2020; Boucher et al., 2018; Vinh et al., 2019; Chen et al., 2020; Li et al., 2018; Ouma et al., 2020; Buma and Lee, 2020; Bande et al., 2018). Many studies have found combinations of Landsat 8 B2, B3, and B4 to be the most frequently used bands (Fadel et al., 2016; Laili et al., 2015; Lim and Choi, 2015; Watanabe et al., 2015; Al-Fahdawi et al., 2015, Patra et al., 2017; Prasad et al., 2020; Malahlela et al., 2018; Yang and Anderson, 2016., 2019; Vinh et al., 2019; Li et al., 2018). This is also the case in this study, where B2, B3, and B4 obtained good correlations with in-situ chl-a; but in addition, B1 for both radiance and reflectance values (Table 4.1.).

Overall, the strongest correlation was found between B4:B1 radiance/reflectance and in-situ chl-a, though Landsat 8 radiance data performed better than Landsat 8 reflectance data.

4.3.1.2. Correlation between Landsat 8 radiance/reflectance and in-situ TSS

In-situ correlations of 0.8 and greater between TSS and Landsat 8 radiance were obtained from bands B1 to B5, and band ratios B1:B2, B1:B3, B1:B4, B2:B1, B2:B3, B2:B4, B3:B1, B3:B2, B4:B1, B4:B2, B3:B4, B5:B4, B3:B5, B4:B5, and B5:B3. In relation to Landsat 8 reflectance values, bands B1, B2 and band ratios B2:B1, B6:B1, B7:B2, B3:B4, B1:B5, B2:B5, B3:B5, B4:B5, B6:B5, B7:B5, B1:B6, B2:B6, B5:B6, B1:B7, B2:B7, B3:B1, B4:B1, B7:B1, B1:B2, B3:B2, B4:B2, B1:B3, B2:B3, B4:B3, B1:B4, and B2:B4 obtained a correlation coefficient of 0.8 and more with in-situ TSS. The correlation results both relate and differ from the findings of other studies, which found that Landsat 8 B2, B3, B4, B5, and their combinations have been commonly used and successful in estimating TSS (Lim and Choi, 2015; Laili et al., 2015; Al-Fahdawi et al., 2015; Larson et al., 2021; Yepez et al., 2018; Pham et al., 2018; Ouma et al., 2020; Sharaf El Din, 2020); however, this study also found that B1, B6, and B7 can also be used to retrieve TSS.

Overall, the strongest correlations between Landsat 8 radiance/reflectance and in-situ TSS were found in B1 for radiance (R = 0.977), and B1 and B2 for reflectance (R = 0.928).

4.3.2 Sentinel 2

Table 4.2 presents the Pearson correlation (R-value) between Sentinel 2 TOA reflectance and in-situ chl-a/TSS and Sentinel 2 BOA reflectance and in-situ chl-a/TSS. The values highlighted in bold indicate correlations of 0.8 and higher.

Table 4.2: Correlations between Sentinel 2 band/band ratio TOA and BOA reflectance with in-situ chl-a and TSS

	TOA		**BOA**	
Band/Band Ratio	**Chl-a**	**TSS**	**Chl-a**	**TSS**
B1	-0.092	0.310	**0.903**	**-0.950**
B2	0.194	-0.201	0.208	-0.435
B3	**0.910**	**-0.859**	0.341	-0.553
B4	**0.902**	**-0.819**	0.346	-0.549
B5	**0.807**	-0.670	**0.843**	-0.742
B6	0.658	-0.466	0.736	-0.584
B7	0.681	-0.509	0.730	-0.588
B8	0.643	-0.452	0.313	-0.217
B8a	0.687	-0.507	0.717	-0.571
B9	-0.043	-0.003	-	-
B10	-0.673	0.788	-	-
B11	0.574	-0.336	0.654	-0.461
B12	0.432	-0.265	0.532	-0.392
B2:B1	0.145	-0.275	-0.085	-0.143
B3:B1	0.165	-0.330	0.122	-0.358
B4:B1	0.159	-0.319	0.119	-0.346
B5:B1	0.211	-0.348	0.774	-0.632
B6:B1	0.138	-0.275	0.403	-0.172
B7:B1	0.149	-0.287	0.285	-0.061
B8:B1	0.161	-0.288	-0.035	0.085
B8a:B1	0.159	-0.291	0.315	-0.129
B9:B1	-0.024	-0.137	-	-
B10:B1	-0.138	-0.018	-	-
B11:B1	0.146	-0.262	-0.399	0.574
B12:B1	0.103	-0.240	-0.546	0.658
B1:B2	-0.395	0.526	0.250	-0.184
B3:B2	0.664	-0.641	**0.865**	**-0.933**
B4:B2	0.635	-0.581	**0.883**	**-0.913**
B5:B2	0.661	-0.538	**0.828**	-0.686
B6:B2	0.409	-0.234	0.511	-0.263
B7:B2	0.463	-0.307	0.389	-0.154
B8:B2	0.462	-0.281	-0.023	0.072
B8a:B2	0.501	-0.335	0.409	-0.215
B9:B2	-0.103	0.052	-	-
B10:B2	-0.709	0.789	-	-
B11:B2	0.331	-0.116	-0.338	0.539
B12:B2	0.172	-0.039	-0.480	0.617
B1:B3	-0.788	**0.889**	-0.714	**0.852**
B2:B3	0.011	-0.019	**-0.820**	**0.921**
B4:B3	-0.463	0.635	-0.191	0.330

	TOA		BOA	
B5:B3	0.323	-0.056	0.476	-0.160
B6:B3	-0.465	0.687	-0.229	0.514
B7:B3	-0.367	0.580	-0.407	0.648
B8:B3	-0.237	0.482	-0.140	0.178
B8a:B3	-0.164	0.387	-0.216	0.407
B9:B3	-0.255	0.209	-	-
B10:B3	**-0.825**	**0.897**	-	-
B11:B3	-0.291	0.490	-0.654	**0.805**
B12:B3	-0.348	0.446	-0.688	**0.809**
B1:B4	-0.780	**0.867**	-0.703	**0.811**
B2:B4	0.027	-0.041	**-0.838**	**0.909**
B3:B4	0.446	-0.615	0.154	-0.294
B5:B4	0.522	-0.307	0.535	-0.263
B6:B4	-0.419	0.634	-0.209	0.483
B7:B4	-0.286	0.484	-0.396	0.626
B8:B4	-0.151	0.386	-0.139	0.177
B8a:B4	-0.063	0.268	-0.197	0.382
B9:B4	-0.229	0.176	-	-
B10:B4	**-0.828**	**0.891**	-	-
B11:B4	-0.234	0.422	-0.658	0.799
B12:B4	-0.304	0.390	-0.681	0.790
B1:B5	**-0.801**	**0.840**	**-0.848**	0.788
B2:B5	0.004	-0.030	-0.297	0.060
B3:B5	-0.271	-0.015	-0.107	-0.159
B4:B5	-0.530	0.300	-0.120	-0.139
B6:B5	-0.797	**0.853**	-0.598	0.717
B7:B5	-0.761	0.788	-0.726	**0.811**
B8:B5	-0.642	0.743	-0.196	0.214
B8a:B5	-0.484	0.545	-0.471	0.534
B9:B5	-0.241	0.175	-	-
B10:B5	**-0.841**	**0.878**	-	-
B11:B5	-0.435	0.539	-0.790	**0.856**
B12:B5	-0.413	0.441	-0.751	0.798
B1:B6	-0.650	0.665	-0.344	0.176
B2:B6	0.087	-0.118	-0.150	-0.108
B3:B6	0.528	-0.741	-0.002	-0.272
B4:B6	0.499	-0.704	-0.010	-0.259
B5:B6	0.790	**-0.834**	0.626	-0.733
B7:B6	0.428	-0.506	-0.349	-0.329
B8:B6	0.538	-0.434	-0.133	0.137
B8a:B6	0.584	-0.566	-0.047	0.007
B9:B6	-0.157	0.082	-	-
B10:B6	**-0.804**	**0.824**	-	-
B11:B6	0.007	0.120	-0.655	0.680
B12:B6	-0.128	0.144	-0.585	0.598
B1:B7	-0.673	0.704	-0.203	-0.026
B2:B7	0.074	-0.102	-0.104	-0.152
B3:B7	-0.450	-0.663	0.022	-0.291
B4:B7	0.379	-0.573	0.018	-0.282
B5:B7	0.755	-0.780	0.755	-0.837

	TOA		BOA	
B6:B7	-0.411	0.494	0.282	-0.241
B8:B7	0.181	-0.001	-0.089	0.098
B8a:B7	0.328	-0.260	0.182	-0.187
B9:B7	-0.175	0.105	-	-
B10:B7	-0.786	**0.821**	-	-
B11:B7	-0.107	0.244	-0.601	0.639
B12:B7	-0.193	0.222	-0.579	0.593
B1:B8	-0.674	0.681	-0.220	0.053
B2:B8	0.069	-0.102	-0.123	-0.133
B3:B8	0.372	-0.620	0.020	-0.296
B4:B8	0.291	-0.525	0.016	-0.286
B5:B8	0.659	-0.755	0.649	-0.743
B6:B8	-0.532	0.445	0.190	-0.176
B7:B8	-0.183	0	-0.094	0.079
B8a:B8	0.244	-0.309	0.179	-0.218
B9:B8	-0.173	0.098	-	-
B10:B8	-0.795	**0.817**	-	-
B11:B8	-0.162	0.259	-0.606	0.640
B12:B8	-0.220	0.221	-0.515	0.528
B1:B8a	-0.691	0.708	-0.332	0.234
B2:B8a	0.053	-0.083	-0.153	-0.090
B3:B8a	0.258	-0.483	-0.015	-0.248
B4:B8a	0.148	-0.350	-0.021	-0.238
B5:B8a	0.510	-0.570	0.492	-0.545
B6:B8a	-0.580	0.576	-0.068	0.130
B7:B8a	-0.368	0.308	-0.317	0.356
B8:B8a	-0.261	0.329	-0.141	0.155
B9:B8a	-0.196	0.125	-	-
B10:B8a	-0.785	**0.811**	-	-
B11:B8a	-0.284	0.410	-0.618	0.666
B12:B8a	-0.283	0.295	-0.526	0.549
B1:B9	-0.076	0.060	-	-
B2:B9	0.118	-0.153	-	-
B3:B9	0.200	-0.245	-	-
B4:B9	0.170	-0.207	-	-
B5:B9	0.238	-0.249	-	-
B6:B9	0.095	-0.104	-	-
B7:B9	0.120	-0.131	-	-
B8:B9	0.131	-0.130	-	-
B8a:B9	0.152	-0.155	-	-
B10:B9	-0.192	0.172	-	-
B11:B9	0.088	-0.075	-	-
B12:B9	0.061	-0.066	-	-
B1:B10	-0.578	-0.545	-	-
B2:B10	0.267	-0.288	-	-
B3:B10	**0.859**	**-0.876**	-	-
B4:B10	**0.857**	**-0.857**	-	-
B5:B10	**0.821**	-0.757	-	-
B6:B10	0.755	-0.672	-	-
B7:B10	0.760	-0.682	-	-

	TOA		BOA	
B8:B10	0.736	-0.632	-	-
B8a:B10	0.759	-0.667	-	-
B9:B10	0.063	-0.131	-	-
B11:B10	0.750	-0.607	-	-
B12:B10	0.703	-0.614	-	-
B1:B11	-0.525	0.488	0.444	0.691
B2:B11	0.082	-0.127	0.023	-0.298
B3:B11	0.315	-0.553	0.155	-0.437
B4:B11	0.255	-0.473	0.154	-0.430
B5:B11	0.453	-0.580	0.778	**-0.844**
B6:B11	-0.023	-0.104	0.717	-0.724
B7:B11	0.098	-0.250	0.650	-0.685
B8:B11	0.167	-0.263	0.147	-0.143
B8a:B11	0.278	-0.415	0.697	-0.729
B9:B11	-0.144	0.061	-	-
B10:B11	-0.695	0.687	-	-
B12:B11	-0.162	0.092	-0.297	0.248
B1:B12	-0.155	0.163	0.523	-0.684
B2:B12	-0.021	0.008	0.088	-0.353
B3:B12	-0.037	0.023	0.245	-0.511
B4:B12	-0.048	0.039	0.246	-0.505
B5:B12	-0.015	0.017	0.745	-0.749
B6:B12	-0.079	0.086	0.684	-0.623
B7:B12	-0.068	0.073	0.630	-0.587
B8:B12	-0.063	0.073	0.226	-0.188
B8a:B12	-0.052	0.059	0.693	-0.651
B9:B12	-0.151	0.120	-	-
B10:B12	-0.201	0.211	-	-
B11:B12	-0.078	0.096	0.257	-0.176

4.3.2.1. Correlation between Sentinel 2 TOA/BOA reflectance and in-situ chl-a

Sentinel 2 TOA reflectance of bands B1, B3, B4, B5, and band ratios B10:B3, B10:B4, B1:B5, B10:B5, B10:B6, B3:B10, B4:B10, and B5:B10 obtained a correlation coefficient of 0.8 and more with in-situ chl-a. In relation to Sentinel 2 BOA reflectance, B1, B5, B3:B2, B4:B2, B5:B2, B2:B3, B2:B4, and B1:B5 achieved correlations of 0.8 and higher with in-situ chl-a. Sentinel 2 B1, B2, B3, B4, B5 and its band combinations displayed the strongest correlations with in-situ chl-a, with TOA reflectance achieving stronger correlations than BOA reflectance data (Table 4.2.). These findings are supported by the studies of Ha et al. (2017), Toming et al. (2016), Grendaitė et al. (2018), Molkov et al. (2019), Pirasteh et al. (2020), Sòria-Perpinyà et al. (2021), Bande et al., (2018); however, this study also found B10 sensitive to chl-a. Ansper and Alikas (2019) and Chen et al. (2017) found that a B8:B4 ratio worked well in chl-a estimation, Ouma et al. (2020) used B3 and B11, and Buma and Lee (2020) found that combinations of B5 to B7 correlated with in-situ chl-a. These studies reveal that there is considerable variation from study to study on which bands can be used to estimate chl-a from Sentinel 2, providing opportunities for more studies to determine which possible Sentinel 2 bands/band combinations can best retrieve chl-a.

Overall, the strongest correlation between Sentinel 2 bands and in-situ chl-a were in B3 TOA (R = 0.91) and B1 BOA (R = 0.903) reflectance.

4.3.2.2. Correlation between Sentinel 2 TOA/BOA reflectance and in-situ TSS

Sentinel 2 TOA reflectance values for bands B3, B4, and band ratios B1:B3, B10:B3, B1:B4, B10:B4, B1:B5, B6:B5, B10:B5, B5:B6, B10:B6, B10:B7, B10:B8, B10:B8a, B3:B10, and B4:B10 obtained correlations of 0.8 and more with in-situ TSS, while BOA reflectance for band B1 and band ratios B3:B2, B4:B2, B1:B3, B2:B3, B2:B4, B11:B3, B12:B3, B1:B4, B7:B5, B11:B5, and B5:B11 achieved correlations greater than 0.8 with in-situ TSS.

Overall, the findings of this study show that B1:B3 TOA reflectance (R = 0.889) and B1 BOA reflectance (R = 0.95) obtained the strongest correlations with in-situ TSS. Studies conducted by Liu et al. (2017), Molkov et al. (2019), Wang et al. (2021), Ouma et al. (2020), and Ciancia et al. (2020) found Sentinel 2 B3, B4, B5, B6, B7, B8 and B8a sensitive in TSS retrieval; however, the correlation results of this study found that B1, B2, B10, and B11 can retrieve TSS, but not B6, B7, B8, and B8a as suggested by other studies. It is worth to note that the number of studies conducted on TSS retrieval from Sentinel 2 imagery are fewer than those for chl-a, and therefore more research needs to be conducted on TSS retrieval from Sentinel 2 imagery.

The overall correlation results indicate the Landsat 8 B1 to B5 and Sentinel 2 B1 to B5 can be used in chl-a and TSS retrieval, supporting the evidence found by Matthews (2011), Yepez et al. (2018) and Gholizadeh et al. (2016), which states that the spectral region from 400-750 nm can be used in chl-a retrieval and 400-900 nm can be used for TSS retrieval. However, the correlation results also showed that Sentinel 2 B10 (1375 nm) and B11 (1610 nm) were able to retrieve TSS, which falls out of the 400-900 nm range. Further still, some studies have indicated that Sentinel 2 B6, B7, B8, and B8a can be used to retrieve TSS which was not the case in this study. Similarly, some studies have found that B7, B8 and B11 can be used to retrieve chl-a; however, this was also not supported by the results of this study. Further research is recommended to determine which bands/band ratios are suitable for chl-a and TSS retrieval, particularly using Sentinel 2 imagery, considering the limited number of studies conducted worldwide.

4.4 ALGORITHMS

Section 4.4 presents the algorithms developed from Landsat 8 and Sentinel 2 satellite imagery. The most significant correlations between radiance and reflectance and in-situ chl-a and TSS, discussed in Section 4.3., were used to develop these algorithms for estimating chl-a and TSS from Landsat 8 and Sentinel 2 imagery.

4.4.1 Landsat 8 algorithms

Tables 4.3 to 4.6 show the algorithms generated using Landsat 8 imagery and the most significant correlations between radiance/reflectance and in-situ chl-a and TSS.

Table 4.3: Linear regression algorithms generated using Landsat 8 radiance data and in-situ chl-a

BAND/BAND RATIO	EQUATION	Pearson correlation (R)	Correlation of determination (R^2)	Standard Error (SE) (μg/t)	Validated R value
B1	*y= -48.253+ 1.229x*	0.862	0.742	4.6082	
B2	*y= -36.955+ 1.211x*	0.882	0.777	4.2841	
B3	*y= -13.733+ 0.863x*	0.907	0.823	3.8148	
B4	*y= -15.613+ 1.886x*	0.922	0.850	3.5189	0.933
B5	*y= -25.527+ 8.856x*	0.848	0.720	4.8084	
B2:B1	*y= -207.261+ 266.666x*	0.902	0.813	3.9215	
B3:B1	*y= -28.020+ 67.363x*	0.917	0.841	3.6236	
B4:B1	*y= -32.519+ 151.959x*	0.931	0.866	3.3195	0.930
B1:B2	*y= 229.627-178.687x*	0.900	0.811	3.9492	
B3:B2	*y= -36.023+ 66.875x*	0.917	0.840	3.6315	
B4:B2	***y= -42.730+ 154.423x***	**0.932**	**0.869**	**3.2883**	**0.928**
B1:B3	*y= 49.970-21.556x*	0.906	0.821	3.8442	
B2:B3	*y= 57.817-31.897x*	0.907	0.822	3.8306	
B1:B4	*y= 55.563-12.285x*	0.923	0.852	3.4950	0.938
B2:B4	*y= 65.892-18.626x*	0.926	0.857	3.4350	0.937

Chl-a radiance algorithms produced from B4, B4:B1, B4:B2, B1:B4 and B2:B4 generated high R^2 values (0.85, 0.866. 0.869, 0.852 and 0.857), validating the results. The B4:B2 algorithm obtained the highest R^2 value (0.869) and the lowest standard error (SE) of 3.2883μg/t, indicating the algorithm's accuracy in retrieving chl-a from Landsat 8 imagery. When validated using the remaining 24 samples, the B4:B2 algorithms obtained an R-value of 0.928. The five most successful algorithms all retained R-values greater than 0.9 when validated; however, the SE values were slightly higher than the B4:B2 algorithm, indicating slightly less accuracy. The overall formula of the most successful algorithm for retrieving chl-a from Landsat 8 imagery is:

$$Chl\text{-}a = -42.730 + 154.423\left(\frac{B4}{B2}\right)$$

Table 4.4: Linear regression algorithms generated using Landsat 8 reflectance data and in-situ chl-a

BAND/BAND RATIO	EQUATION	R	R^2	SE (µg/t)	Validated R value
B1	*y= 24.471-172.849x*	0.835	0.698	4.9922	
B2	*y= 25.731-236.698x*	0.822	0.676	5.1708	
B2:B1	*y= -92.531+124.224x*	0.901	0.812	3.9343	0.909
B3:B1	*y= -4.752+15.280x*	0.900	0.811	3.9506	0.925
B4:B1	***y= -6.037+29.579x***	**0.917**	**0.842**	**3.6123**	**0.938**
B1:B2	*y= 117.341-88.045x*	0.906	0.820	3.8487	0.924
B3:B2	*y= -6.577+14.684x*	0.889	0.791	4.1552	
B4:B2	*y= -8.490+29.105x*	0.912	0.831	3.7326	0.933
B1:B3	*y= 25.777-11.110x*	0.871	0.759	4.4572	
B2:B3	*y= 27.465-15.483x*	0.867	0.751	4.5288	
B1:B4	*y= 27.297-7.185x*	0.883	0.780	4.2565	
B2:B4	*y= 29.500-10.170x*	0.881	0.776	4.2985	
B1:B5	*y= 34.062-5.065x*	0.815	0.664	5.2619	

Table 4.4 shows reflectance algorithms developed for chl-a estimation from Landsat 8 imagery. Bands B2:B1, B3:B1, B4:B1, B1:B2, and B4:B2 algorithms generated high R^2 values of 0.812. 0.811, 0.842, 0.820 and 0.831 respectively and were therefore validated. The B4:B1 algorithm obtained the highest R-value (0.938) after validation and a slightly lower SE value (3.6123µg/t) than the other four algorithms. However, all algorithms obtained correlations of 0.9 and more when validated with the remaining 24 samples, indicating their ability to retrieve chl-a from Landsat 8 reflectance data. The overall formula of the most successful reflectance algorithm for retrieving chl-a from Landsat 8 imagery is:

$$Chl\text{-}a = -6.037 + 29.579\left(\frac{B4}{B1}\right)$$

Table 4.5: Linear regression algorithms generated using Landsat 8 radiance data and in-situ TSS

BAND/BAND RATIO	EQUATION	R	R^2	SE (mg/t)	Validated R value
B1	***y= 57.905-0.965x***	**0.977**	**0.955**	**1.3335**	**0.970**
B2	*y= 47.946-0.922x*	0.970	0.941	1.5260	0.959
B3	*y= 29.357-0.624x*	0.947	0.897	2.0130	0.921
B4	*y= 30.080-1.315x*	0.928	0.862	2.3352	
B5	*y= 35.609-5.823x*	0.806	0.649	3.7242	
B2:B1	*y= 163.958-186.244x*	0.910	0.828	2.6094	
B3:B1	*y= 38.830-47.151x*	0.927	0.859	2.3586	
B4:B1	*y= 40.281-100.197x*	0.886	0.786	2.9102	
B1:B2	*y= -142.064+125.521x*	0.914	0.835	2.5566	
B3:B2	*y= 44.658-47.144x*	0.933	0.871	2.2594	
B4:B2	*y= 46.811-101.219x*	0.882	0.779	2.9574	
B1:B3	*y= -16.785+15.632x*	0.949	0.900	1.9842	0.933
B2:B3	*y= -22.493+23.143x*	0.950	0.903	1.9614	0.930
B5:B3	*y= -20.688+214.683x*	0.907	0.823	2.6466	
B1:B4	*y= -19.112+8.450x*	0.917	0.841	2.5098	
B2:B4	*y= -25.742+12.655x*	0.908	0.825	2.6291	
B3:B4	*y= 157.725-72.311x*	0.803	0.644	3.7488	
B5:B4	*y= -25.673+123.614x*	0.889	0.790	2.8812	
B3:B5	*y= 42.877-4.550x*	0.893	0.797	2.8322	
B4:B5	*y= 47.877-10.681x*	0.876	0.768	3.0271	

Algorithms developed using Landsat 8 radiance and in-situ TSS are shown in Table 4.5. Algorithms produced using B1, B2, B3, B1:B3 and B2:B3 generated high R^2 values (0.955, 0.941, 0.897, 0.9 and 0.903) and were validated. The B1 algorithm obtained the highest R-value (0.970) after validation and the lowest SE value (1.3335 mg/t), indicating the ability of the algorithm to retrieve TSS from Landsat 8 accurately. All five algorithms obtained validated R values greater than 0.9 and SE values less than 2 mg/t, indicating both the accuracy and success of the five TSS retrieval algorithms. The overall formula of the most successful radiance algorithm for retrieving TSS from Landsat 8 imagery is:

TSS = 57.905 - 0.965 (B1)

Table 4.6: Linear regression algorithms generated using Landsat 8 reflectance data and in-situ TSS

BAND/BAND RATIO	EQUATION	R	R^2	SE (mg/t)	Validated R value
B1	***y= 0.350+140.827x***	**0.983**	**0.966**	**1.1579**	**0.977**
B2	*y= -0.890+195.916x*	0.983	0.966	1.1662	0.979
B2:B1	*y= 82.013-84.546x*	0.886	0.785	2.9161	
B3:B1	*y= 22.995-11.186x*	0.952	0.906	1.9248	
B4:B1	*y= 23.524-20.861x*	0.935	0.873	2.2374	
B6:B1	*y= 22.647-135.650x*	0.841	0.707	3.4039	
B7:B1	*y= 22.438-216.965x*	0.912	0.832	2.5747	
B1:B2	*y= -61.822+60.736x*	0.902	0.814	2.7092	
B3:B2	*y= 24.635-11.031x*	0.965	0.931	1.6569	
B4:B2	*y= 25.527-20.973x*	0.949	0.900	1.9868	
B7:B2	*y= 23.137-196.744x*	0.888	0.789	2.8866	
B1:B3	*y= -0.062+8.611x*	0.975	0.951	1.3888	0.967
B2:B3	*y= -1.467+12.084x*	0.977	0.954	1.3413	0.970
B4:B3	*y= -84.060+166.974x*	0.900	0.810	2.7424	
B1:B4	*y= -0.978+5.464x*	0.970	0.941	1.5231	
B2:B4	*y= -2.722+7.769x*	0.972	0.945	1.4809	0.960
B3:B4	*y= 103.934-52.687x*	0.888	0.789	2.8863	
B1:B5	*y= -5.919+3.810x*	0.885	0.784	2.9214	
B2:B5	*y= -9.256+5.596*	0.847	0.718	3.3381	
B3:B5	*y= 30.338-4.639x*	0.885	0.783	2.9275	
B4:B5	*y= 33.139-9.424x*	0.854	0.729	3.2705	
B6:B5	*y= 36.222-77.161x*	0.808	0.653	3.7031	
B7:B5	*y= 27.825-81.945x*	0.815	0.665	3.6397	
B1:B6	*y= 0.221+0.712x*	0.895	0.802	2.7981	
B2:B6	*y= -1.042+0.985x*	0.878	0.771	3.0065	
B5:B6	*y= -12.917+7.486x*	0.822	0.675	3.5815	
B1:B7	*y= 1.842+0.350x*	0.898	0.807	2.7630	

Table 4.6 displays the linear regression algorithms produced using Landsat 8 reflectance data and in-situ TSS. TSS reflectance algorithms developed from B1, B2, B1:B3, B2:B3 and B2:B4 generated high R^2 values of 0.966, 0.966, 0.951, 0.970 and 0.945 and were validated. The B1 algorithm obtained the highest R-value (0.977) after validation, indicating the ability of the algorithm to retrieve TSS from Landsat 8. All five algorithms obtained validated R values greater than 0.9, and the SE for all algorithms was less than 2 mg/t, once again indicating both the accuracy and success of the five TSS retrieval algorithms. The overall formula of the most successful algorithm for retrieving TSS from Landsat 8 is:

TSS = 0.350 + 140.827 (B1)

4.4.2 Sentinel 2 algorithms

Tables 4.7 to 4.10 show the algorithms generated using Sentinel 2 imagery and the most significant correlations between TOA/BOA reflectance and in-situ chl-a and TSS.

Table 4.7: Linear regression algorithms generated using Sentinel 2 BOA reflectance and in-situ chl-a

BAND/BAND RATIO	EQUATION	R	R^2	SE (µg/t)	Validated R value
B1	***y= -9.799+ 924.677x***	**0.903**	**0.816**	**3.896**	**0.916**
B5	*y= 0.631+ 487.332x*	0.843	0.711	4.8833	0.891
B3:B2	*y= -18.829+ 21.910x*	0.865	0.749	4.5501	0.891
B4:B2	*y= -21.446+ 47.771x*	0.883	0.779	4.2669	0.803
B5:B2	*y= -7.815+ 29.438x*	0.828	0.685	5.0919	
B2:B3	*y= 37.698- 33.917x*	0.820	0.673	5.1932	
B2:B4	*y= 40.643- 18.960x*	0.838	0.703	4.9158	
B1:B5	*y= 36.722- 18.543x*	0.848	0.719	4.8135	0.826

Table 4.7 displays the algorithms developed using Sentinel 2 BOA reflectance and in-situ chl-a. Algorithms produced from B1, B5, B3:B2, B4:B2 and B1:B5 generated high R^2 values (0.816, 0.711, 0.749, 0.779 and 0.719) and were thus validated. The B1 algorithm was the only algorithm to obtain a R-value greater than 0.9 and a SE value lower than 4µg/t after validation with the remaining 24 samples, indicating that the algorithm can retrieve chl-a from Sentinel 2. The overall formula of the most successful algorithm for retrieving chl-a from Sentinel 2 is:

Chl-a = -9.799 + 924.677 (B1)

Table 4.8: Linear regression algorithms generated using Sentinel 2 TOA reflectance and in-situ chl-a

BAND/BAND RATIO	EQUATION	R	R^2	SE (µg/t)	Validated R value
B3	***y= -25.925+ 502.455x***	**0.910**	**0.828**	**3.7678**	**0.925**
B4	*y= -27.825+ 945.445x*	0.902	0.813	3.9244	0.926
B5	*y= -13.633+ 655.309x*	0.807	0.652	5.3560	
B10:B3	*y= -1438.337+ 132.690x*	0.825	0.681	5.1268	
B10:B4	*y= 31.237-856.439x*	0.828	0.685	5.0933	
B1:B5	*y= 37.502-7.853x*	0.801	0.642	5.4309	
B10:B5	*y= 30.476-716.815x*	0.841	0.708	4.9101	0.903
B10:B6	*y=34.208-778.047x*	0.804	0.646	5.4022	
B3:B10	*y= -9.300+ 0.232x*	0.859	0.738	4.6511	0.886
B4:B10	*y= -9.904+ 0.429x*	0.857	0.735	4.6774	0.885
B5:B10	*y= -5.521+ 0.369x*	0.821	0.674	5.1825	

The bands/band ratios algorithms developed from Sentinel 2 B3, B4, B10:B5, B3:B10, and B4:B10 obtained high R^2 values of 0.828, 0.813, 0.708, 0.738, and 0.735, respectively and were validated (Table 4.8). The B3 algorithm obtained the highest R-value (0.925) and lowest SE value (3.7678µg/t) after validation, indicating the algorithm's ability in chl-a retrieval from Sentinel 2 TOA reflectance data. The overall formula of the most successful algorithm for chl-a retrieval from Sentinel 2 is:

Chl-a = -25.925 + 502.455 (B3)

Table 4.9: Linear regression algorithms generated using Sentinel 2 BOA reflectance and in-situ TSS

BAND/BAND RATIO	EQUATION	R	R^2	SE (mg/t)	Validated R value
B1	***y= 26.496- 663.317x***	**0.950**	**0.902**	**1.9429**	**0.938**
B3:B2	*y= 33.500- 16.127x*	0.933	0.871	2.2225	0.901
B4:B2	*y= 34.489- 33.706x*	0.913	0.833	2.5317	0.882
B1:B3	*y= -8.018+32.784x*	0.852	0.725	3.2468	
B2: B3	*y= -8.954+25.978x*	0.921	0.848	2.4176	0.919
B11: B3	*y= 2.585+57.976x*	0.805	0.648	3.6762	
B12:B3	*y= 3.526+66.062x*	0.809	0.655	3.6403	
B1:B4	*y= -8.126+16.669x*	0.811	0.657	3.6275	
B2:B4	*y= -10.391+14.207x*	0.909	0.826	2.5860	0.890
B7:B5	*y= -4.630+22.016x*	0.811	0.657	3.6268	
B11:B5	*y= 1.512+27.883x*	0.856	0.733	3.2016	
B5:B7	*y= 30.238-12.714x*	0.837	0.701	3.3879	
B5:B11	*y= 22.004-2.876x*	0.844	0.712	3.3251	

Table 4.9 shows the Sentinel 2 BOA reflectance algorithms and in-situ TSS. B1, B3:B2, B4:B2, B2:B3 and B2:B4 algorithms which generated high R^2 values (0.902, 0.871, 0.833, 0.848 and 0.826) and were validated. The B1 algorithm obtained the highest R-value (0.938) and lowest SE value (1.9429 mg/t) after validation, indicating the algorithm's success in retrieving TSS. The overall formula of the most successful algorithm for TSS retrieval from Sentinel 2 is:

TSS = 26.496 -663.317 (B1)

Table 4.10: Linear regression algorithms generated using Sentinel 2 TOA reflectance and in-situ TSS

BAND/BAND RATIO	EQUATION	R	R^2	SE (mg/t)	Validated R value
B3	*y= 35.475-323.529x*	0.859	0.737	3.1769	
B4	*y= 35.816-586.291x*	0.819	0.672	3.5506	
B1:B3	***y= -9.344+ 12.563x***	**0.889**	**0.790**	**2.8363**	**0.926**
B10:B3	*y= -2.664+ 1066.930x*	0.897	0.805	2.7364	0.906
B1:B4	*y= -10.268+ 7.386x*	0.867	0.752	3.0839	
B10:B4	*y= -3.309+ 628.751x*	0.891	0.793	2.8171	0.888
B6:B5	*y= -36.668+ 54.763x*	0.853	0.728	3.2305	
B10:B5	*y= -2.295+ 510.829x*	0.878	0.772	2.9602	0.886
B5:B6	*y= 57.560-39.957x*	0.834	0.696	3.4169	
B10:B6	*y= -4.635+ 544.474x*	0.824	0.679	3.5080	
B10:B7	*y= -3.357+ 487.930x*	0.821	0.673	3.5411	
B10:B8	*y= -3.321+ 391.806x*	0.817	0.667	3.5751	
B10:B8a	*y= -2.106+ 351.510x*	0.811	0.658	3.6234	
B3:B10	*y= 25.739-0.161x*	0.876	0.767	2.9901	0.827
B4:B10	*y= 25.903-0.293x*	0.857	0.735	3.1891	

Algorithms developed using Sentinel 2 TOA, and in-situ TSS are shown in Table 4.10. Band ratio algorithms B1:B3, B10:B3, B10:B4, B10:B5 and B3:B10 generated high R^2 values of 0.790, 0.805, 0.793, 0.772 and 0.767 and were validated. The B1:B3 algorithm obtained the highest R-value (0.926) and a low SE value (2.8363 mg/t) after validation, indicating the algorithm's success in retrieving TSS. The overall formula of the most successful algorithm for TSS retrieval from Sentinel 2 is:

$$TSS = -9.344 + 12.563 \left(\frac{B1}{B3}\right)$$

This study compared algorithms generated using Landsat 8 radiance and reflectance data and Sentinel 2 BOA and TOA reflectance, which has rarely been done before.
Algorithms developed from Landsat 8 radiance and reflectance achieved good results (R^2 > 0.8), while algorithms developed using Sentinel 2 TOA, and BOA reflectance also obtained good results (R^2 > 0.79), with TOA reflectance algorithms generating better results (R^2 = 0.828) than BOA reflectance algorithms (R^2 = 0.816) for chl-a, while for TSS BOA reflectance obtained better results (R^2 > 0.902) than TOA reflectance algorithms (R^2 > 0.790).

The algorithms developed using Landsat 8 data were more successful than those created using Sentinel 2. Algorithms developed using Landsat 8 had higher R-values, R^2-values, and lower SE values indicating the success of Landsat 8 in developing chl-a and TSS retrieval models. Sentinel 2 can also retrieve chl-a and TSS remotely; however, the algorithms obtained had slightly lower R-values, R^2-values, and higher SE values, indicating possible overestimation or underestimation of chl-a and TSS with algorithms developed from Sentinel 2. The Landsat 8 algorithms for estimating TSS were more accurate than those for estimating chl-a, possibly due to the higher Signal-to-Noise Ratio (SNR) and bandwidth placement of Landsat 8 satellites (Ouma et al., 2020). At the same time, there was no noticeable difference in the chl-a and TSS estimation from Sentinel 2 imagery.
Yadav et al. (2019), Buma and Lee (2020), Watanabe et al. (2017), and Bande et al. (2018) found that Sentinel 2 outperformed Landsat in chl-a and TSS estimation; however, Ouma et al. (2020) found that Landsat 8 outperformed Sentinel 2 in TSS estimation, but there was no significant difference in chl-a retrieval between the two satellites. Ciancia et al. (2020) combined Landsat 8 and Sentinel 2 information to estimate TSS with good results; however, a comparison for TSS retrieval between the satellites was not performed. The results of studies conducted elsewhere show that Sentinel is better able to retrieve chl-a and TSS; however, Ouma et al. (2020) and this study revealed that Landsat 8 performed better in chl-a and TSS estimation. Many studies have been conducted using Landsat 8 for water quality parameter estimation (Sharaf El Din, 2020; Markogianni et al., 2017; Prasad et al., 2020; Ledesma et al., 2019, Hu et al., 2021; Zhang et al., 2020; Malahlela et al., 2018; Peterson et al., 2018; Kurniadin and Jaelani, 2016; Fadel et al., 2016; Patra et al., 2017; Kim et al., 2016; Lim and Choi, 2015; Masocha et al., 2018; Liu et al., 2017; Sharaf El Din and Zhang, 2017; Laili et al., 2015), but fewer studies have considered Sentinel 2 (Soomets et al., 2020; Bresciani et al., 2018; Li et al., 2021; Grendaitė et al., 2018; Sòria-Perpinyà et al., 2020; Ansper and Alikas, 2019; Molkov et al., 2019; Pirasteh et al., 2010), and fewer still have compared Landsat 8 and Sentinel 2 for water quality monitoring (Ouma et al., 2020; Yadav et al., 2019; Buma and Lee, 2020; Watanabe et al., 2017; Bande et al., 2018).
More studies should be conducted locally and internationally to validate the results found in this and other studies, considering that few studies have been conducted on Sentinel 2 and water quality estimation compared to Landsat 8. Chl-a has also been extensively studied compared to other water quality parameters, leaving room for more studies in other remotely sensed water quality parameters.

4.5 SURFACE DISTRIBUTION OF CHL-A AND TSS IN THE INANDA DAM

Maps showing the surface distribution of chl-a/TSS (Section 4.5) were produced using the most successful chl-a and TSS algorithms developed from Landsat 8 radiance and reflectance, and Sentinel 2 TOA and BOA reflectance, and in-situ chl-a/TSS concentrations (Section 4.4).

4.5.1 Surface distribution of Chl-a from Landsat 8 and Sentinel 2

Figure 4.7(a) displays the distribution of in-situ chl-a in the Inanda Dam, showing the highest chl-a concentrations along the narrow inlet of the Dam, with chl-a concentrations decreasing as the Dam widens and water flows along the Dam towards the dam wall. While the general trend of chl-a indicates the highest concentrations at the entrance of the Dam, decreasing as water flows through the Dam, there is some variation in this distribution, as indicated by points x, y, and z in Figure 4.7(a). At point x, there is a considerable decrease in chl-a concentrations, while at point y, the chl-a concentrations start to increase, with the higher concentrations found along the dam edge. Point z shows a slight increase in chl-a concentrations, with chl-a decreasing as water flows after point z towards the dam wall.

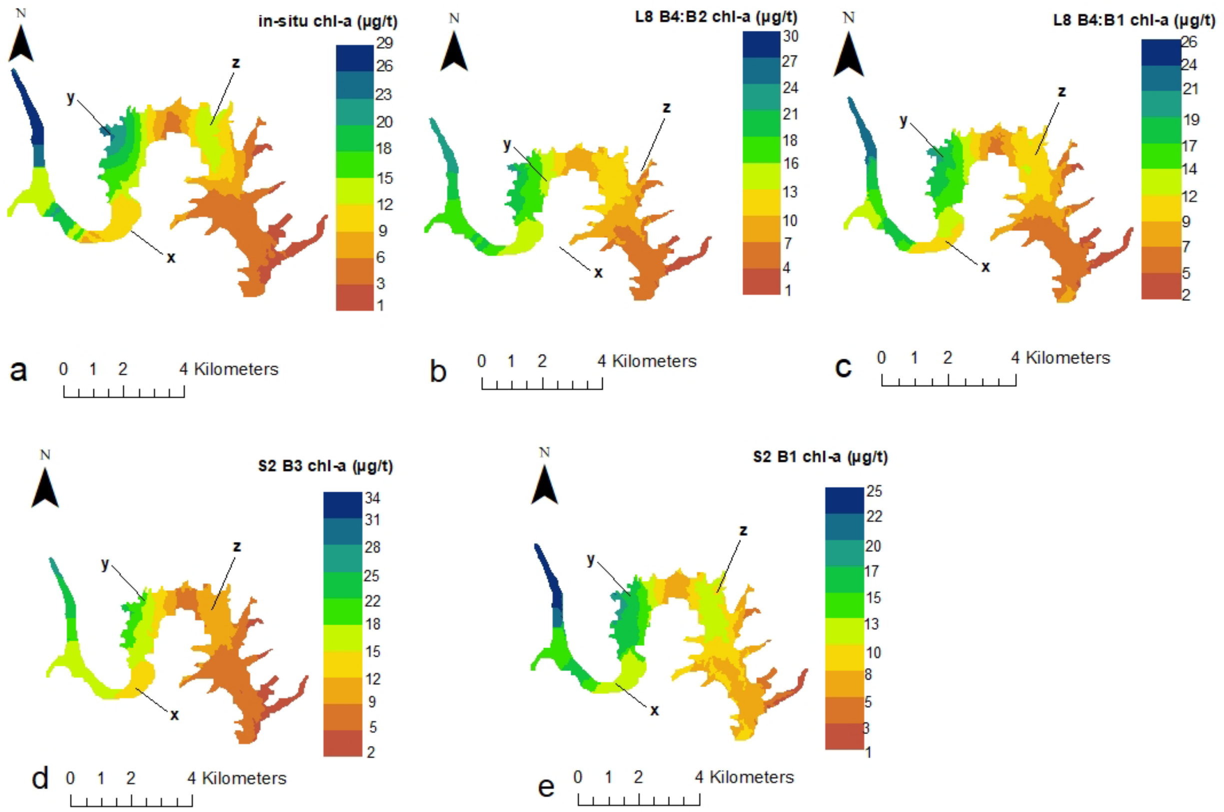

Figure 4.7. Surface distribution of chl-a according to (a) in-situ chl-a, (b) Landsat 8 B4:B2 radiance algorithm, (c) Landsat 8 B4:B1 reflectance algorithm, (d) Sentinel 2 B3 TOA reflectance algorithm, and (e) Sentinel 2 B1 BOA reflectance algorithm

Figures 4.7(b) to (e) shows a similar general chl-a trend and variations in surface distribution as in the case of in-situ data (Figure 4.7(a); however, Figure 4.7(c) shows that the Landsat 8 B4:B1 reflectance algorithm underestimated the chl-a concentrations upstream at the dam inlet but overestimated the chl-a concentration downstream closer to the dam wall. The Sentinel 2 B3 TOA algorithm, while showing the correct trend in chl-a distribution over the Dam, overestimated the chl-a concentrations in the Dam (Figure 4.7. (d)). The Sentinel 2 B1 BOA algorithm (Figure 4.7. (e)) was not able to estimate higher chl-a concentrations and therefore underestimated chl-a at the Dam inlet but accurately estimated the lower chl-a concentrations downstream closer to the outlet (Dam wall). The Landsat 8 B4:B2 radiance algorithm estimated chl-a values which closely resembled the in-situ values, with a difference of ± 1µg/t on either end of the range, indicating that this algorithm can accurately estimate the chl-a in the Dam, while also capturing the variations in chl-a distribution over the Dam (Figure 4.7. (b)). Overall, the Landsat 8 B4:B2 radiance algorithm produced a chl-a surface distribution map that closely resembled the map produced using in-situ chl-a data.

The distribution pattern of chl-a in the Inanda Dam may be attributed to many factors, which need to be further examined to determine their validity. Darvill Wastewater Works and the Cato Ridge Abattoir are located north of the dam and release high amounts of nutrients which find their way into the Inanda Dam (Graham, 2004; Simpson and Pillay, 2000). The dam retains approximately 80% of the nutrient load, and the dam's meandering nature and prevailing easterly wind keeps the nutrient load (phosphorous) trapped upstream, leading to more chl-a forming upstream and hence higher chl-a concentrations found at the dam entrance (Graham, 2004). As water flows through the dam towards the dam outlet, the chl-a concentrations decrease, possibly due to the widening of the dam, however more research must be conducted to determine the accuracy of this statement.

4.5.2 Surface distribution of TSS from Landsat 8 and Sentinel 2

Figure 4.8(a) displays the distribution of in-situ TSS concentrations over the Inanda dam, showing the variation of TSS concentrations in the Dam. Concentrations are, however, generally lower near the dam inlet and higher closer to the dam wall and along the dam edges, with TSS values ranging from 4 mg/t to 18 mg/t. Figures 4.8. (b) to (e) show that all the algorithms were able to produce the surface distribution of TSS, capturing the trend and variation of TSS over in the Dam, with the Landsat 8 B1 radiance algorithm most successful in producing a surface distribution map to capture TSS as per in-situ data.

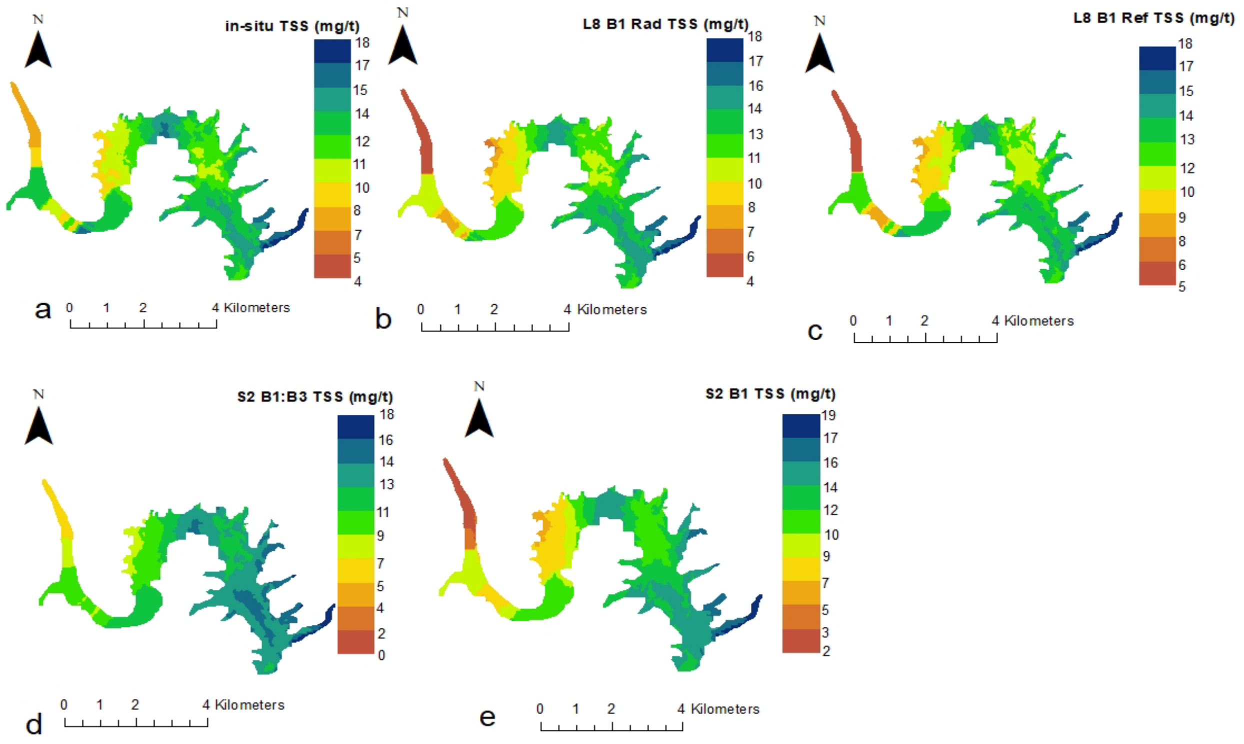

Figure 4.8. Surface distribution of TSS according to (a) in-situ data, (b) Landsat 8 B1 radiance algorithm, (c) Landsat 8 B1 reflectance algorithm, (d) Sentinel 2 B1:B3 TOA reflectance algorithm, and (e) Sentinel 2 B1 BOA reflectance algorithm

The Landsat 8 B1 reflectance algorithm had slight difficulty estimating lower values of TSS; however, it accurately estimated high TSS concentrations, capturing some TSS variation over the Dam, though not as accurately as the Landsat 8 radiance B1 algorithm. Sentinel 2 B1:B3 TOA and B1 BOA reflectance algorithm underestimated TSS concentrations, particularly for lower TSS concentrations, but captured TSS variation in the Dam.

Variation of TSS distribution in the Inanda Dam can be due to many factors such as temperature, rainfall, wind, human acitvities, streamflow, climatic variation, sediment availability, resuspended riverbed material, the underlying geology of the area, and much more (Jaiyeola, 2015; Bayram and Kenanoğlu, 2016), however more research must be conducted in the Inanda Dam to determine which of these factors or combination of factors are responsible for the distribution of TSS in the dam.

CHAPTER 5: CONCLUSIONS AND RECOMMENDATIONS

5.1 CONCLUSIONS

This study evaluated the ability of algorithms for retrieving chl-a and TSS from Landsat 8 and Sentinel 2 satellites and mapped their surface distribution in the Inanda Dam. In-situ chl-a and TSS water samples were collected from the Dam during the wet and dry seasons. The in-situ samples and radiance and reflectance values from Landsat 8 and Sentinel 2 were used to develop statistical algorithms to estimate chl-a and TSS.
This study consisted of five deliverables (objectives) to fulfil a contract funded by the Water Research Commission (WRC) of South Africa. They included 1) developing wet season algorithms for retrieving chl-a and TSS from Landsat 8 and Sentinel 2 images in the Inanda Dam, 2) developing dry season algorithms for retrieving chl-a and TSS from Landsat 8 and Sentinel 2 images in the Inanda Dam, 3) mapping the surface distribution of chl-a in the Inanda Dam, 4) mapping the surface distribution of TSS in the Dam, and 5) produce a full report of the study. Overall, the aim and objectives of this study (Sections 1.2 and 1.3) were achieved (Chapters 3 and 4) and are summarized as follows:

- Chl-a was extracted from Landsat 8 and Sentinel 2 imagery.
- TSS was extracted from Landsat 8 and Sentinel 2 imagery.
- Landsat 8 obtained better retrieval results than Sentinel 2 for chl-a and TSS.
- In addition, both single bands and band ratios could estimate water quality parameters.
- Both Landsat 8 radiance and reflectance values successfully generated algorithms for extracting chl-a and TSS in the Inanda Dam.
- Sentinel 2 BOA algorithms performed better in TSS retrieval, and Sentinel 2 TOA algorithms were more successful in chl-a retrieval.
- Surface distribution maps were produced showing the spatial distribution of chl-a and TSS concentrations in the Dam.

5.2 RECOMMENDATIONS

Further studies should be conducted on the water and wind circulation patterns in and on the surface of the Dam to understand their roles on distribution of chl-a and TSS in the Dam. Future studies on remote sensing of water quality in the Inanda Dam should explore the integration of hyperspectral ASD data to improve the accuracy and quality of results. More studies need to be carried out in other South African water bodies to further strengthen the slowly growing data on algorithms to monitor chl-a, TSS, and other water quality parameters. Thus far, few studies have been conducted on water quality and remote sensing, and fewer still on the use of Landsat 8 and Sentinel 2. The new Landsat 9 satellite, which was launched on the 27th of September 2021, along with the already orbiting Landsat 8, Sentinel 2A, and Sentinel 2B satellites, can provide an improved free data source. Scientists can use this information to monitor water quality almost daily to ensure the sustainability of South Africa's freshwater resources. With modern advancements in artificial intelligence and machine learning, opportunities exist for developing apps to monitor different water quality parameters in South African bodies in real-time.

REFERENCES

Agunbiade, F.O. and Moodley, B. (2014). Pharmaceuticals as emerging organic contaminants in Umgeni River water system, KwaZulu-Natal, South Africa. *Environmental monitoring and assessment*, *186*(11), pp.7273-7291.

Alcântara, E., Bernardo, N., Watanabe, F., Rodrigues, T., Rotta, L., Carmo, A., Shimabukuro, M., Gonçalves, S. and Imai, N. (2016). Estimating the CDOM absorption coefficient in tropical inland waters using OLI/Landsat-8 images. *Remote Sensing Letters*, *7*(7), pp.661-670.

Al-Fahdawi, A.A., Rabee, A.M. and Al-Hirmizy, S.M. (2015). Water quality monitoring of Al-Habbaniyah Lake using remote sensing and in situ measurements. *Environmental monitoring and assessment*, *187*(6), pp.1-11.

Al-Kharusi, E.S., Tenenbaum, D.E., Abdi, A.M., Kutser, T., Karlsson, J., Bergström, A.K. and Berggren, M. (2020). Large-scale retrieval of coloured dissolved organic matter in northern lakes using Sentinel-2 data. *Remote Sensing*, *12*(1), p.157.

Ansari, M. and Akhoondzadeh, M. (2020). Mapping water salinity using Landsat-8 OLI satellite images (Case study: Karun basin located in Iran). *Advances in Space Research*, *65*(5), pp.1490-1502.

Ansper, A. and Alikas, K. (2019). Retrieval of chlorophyll a from Sentinel-2 MSI data for the European Union water framework directive reporting purposes. *Remote Sensing*, *11*(1), p.64.

Aptoula, E. and Ariman, S. (2021). Chlorophyll-a Retrieval From Sentinel-2 Images Using Convolutional Neural Network Regression. *IEEE Geoscience and Remote Sensing Letters*.

Bande, P., Adam, E., Elbasit, M.A.A. and Adelabu, S. (2018), July. Comparing Landsat 8 and Sentinel-2 in mapping water quality at Vaal dam. In *Proceedings of the International Geoscience and Remote Sensing Symposium (IGARSS), Valencia, Spain* (pp. 22-27).

Bayram, A. and Kenanoğlu, M. (2016). Variation of total suspended solids versus turbidity and Secchi disk depth in the Borçka Dam Reservoir, Çoruh River Basin, Turkey. *Lake and reservoir management*, *32*(3), pp.209-224.

Bonansea, M., Ledesma, M., Bazán, R., Ferral, A., German, A., O'Mill, P., Rodriguez, C. and Pinotti, L. (2019). Evaluating the feasibility of using Sentinel-2 imagery for water clarity assessment in a reservoir. *Journal of South American Earth Sciences*, *95*, p.102265.

Boucher, J., Weathers, K.C., Norouzi, H. and Steele, B. (2018). Assessing the effectiveness of Landsat 8 chlorophyll a retrieval algorithms for regional freshwater monitoring. *Ecological applications*, *28*(4), pp.1044-1054.

Bresciani, M., Cazzaniga, I., Austoni, M., Sforzi, T., Buzzi, F., Morabito, G. and Giardino, C. (2018). Mapping phytoplankton blooms in deep subalpine lakes from Sentinel-2A and Landsat-8. *Hydrobiologia*, *824*(1), pp.197-214.

Buma, W.G. and Lee, S.I. (2020). Evaluation of sentinel-2 and landsat 8 images for estimating chlorophyll-a concentrations in Lake Chad, Africa. *Remote Sensing*, *12*(15), p.2437.

Cairo, C., Barbosa, C., Lobo, F., Novo, E., Carlos, F., Maciel, D., Flores Júnior, R., Silva, E. and Curtarelli, V. (2020). Hybrid chlorophyll-a algorithm for assessing trophic states of a tropical Brazilian reservoir based on MSI/Sentinel-2 data. *Remote Sensing*, *12*(1), p.40.

Chen, J., Zhu, W.N., Tian, Y.Q. and Yu, Q. (2017). Estimation of colored dissolved organic matter from Landsat-8 imagery for complex inland water: case study of Lake Huron. *IEEE Transactions on Geoscience and Remote Sensing*, *55*(4), pp.2201-2212.

Chen, J., Zhu, W., Pang, S. and Cheng, Q. (2019). Applicability evaluation of Landsat-8 for estimating low concentration colored dissolved organic matter in inland water. *Geocarto International*, pp.1-15.

Chen, X., Liu, L., Zhang, X., Li, J., Wang, S., Liu, D., Duan, H. and Song, K. (2021). An Assessment of Water Color for Inland Water in China Using a Landsat 8-Derived Forel-Ule Index and the Google Earth Engine Platform. *IEEE Journal of Selected Topics in Applied Earth Observations and Remote Sensing*, *14*, pp.5773-5785.

Ciancia, E., Campanelli, A., Lacava, T., Palombo, A., Pascucci, S., Pergola, N., Pignatti, S., Satriano, V. and Tramutoli, V. (2020). Modeling and multi-temporal characterization of total suspended matter by the combined use of Sentinel 2-MSI and Landsat 8-OLI data: The Pertusillo Lake case study (Italy). *Remote Sensing*, *12*(13), p.2147.

Concha, J.A. and Schott, J.R. (2016). Retrieval of color producing agents in Case 2 waters using Landsat 8. *Remote sensing of Environment*, *185*, pp.95-107.

Deutsch, E., Alameddine, I. and El-Fadel, M. (2014). Developing Landsat Based Algorithms to Augment in Situ Monitoring of Freshwater Lakes and Reservoirs.

Donnenfeld, Z., Crookes, C. and Hedden, S. (2018*). A delicate balance: Water scarcity in South Africa*. 13. South Africa: Water Research Commission.

Dörnhöfer, K., Göritz, A., Gege, P., Pflug, B. and Oppelt, N. (2016). Water constituents and water depth retrieval from Sentinel-2A—A first evaluation in an oligotrophic lake. *Remote Sensing*, *8*(11), p.941.

Elangovan, A. and Murali, V. (2020). Mapping the chlorophyll-a concentrations in hypereutrophic Krishnagiri Reservoir (India) using Landsat 8 Operational Land Imager. *Lakes & Reservoirs: Research & Management*, *25*(4), pp.377-387.

European Space Agency. (2021). Spatial Resolution. Available at: https://sentinels.copernicus.eu/web/sentinel/user-guides/sentinel-2-msi/resolutions/spatial. (Accessed 01 June 2021)

Fadel, A., Faour, G. and Slim, K. (2016). Assessment of the trophic state and chlorophyll-a concentrations using Landsat OLI in Karaoun reservoir, Lebanon. *Leban. Sci. J*, *17*(2), pp.130-145.

Fischer, F., Hamdan, Y., Hansson, A., Josefsson, E. and Sundström, L. (2019). *Water quality modelling and quantitative microbial risk assessment of Msunduzi River* (Bachelor's thesis).

Gholizadeh, M. H., Melesse, A. M. and Reddi, L. A. (2016). Comprehensive Review on Water Quality Parameters Estimation Using Remote Sensing Techniques. *Sensors*, 16 (8), p.p.1298.

Giardino, C., Bresciani, M., Cazzaniga, I., Schenk, K., Rieger, P., Braga, F., Matta, E. and Brando, V.E. (2014). Evaluation of multi-resolution satellite sensors for assessing water quality and bottom depth of Lake Garda. *Sensors*, *14*(12), pp.24116-24131.

González-Márquez, L.C., Torres-Bejarano, F.M., Torregroza-Espinosa, A.C., Hansen-Rodríguez, I.R. and Rodríguez-Gallegos, H.B. (2018). Use of LANDSAT 8 images for depth and water quality assessment of El Guájaro reservoir, Colombia. *Journal of South American Earth Sciences*, *82*, pp.231-238.

Graham, P.M. (2004). *Modelling the water quality in dams within the Umgeni Water operational area with emphasis on algal relations* (Doctoral dissertation, North-West University).

Grendaitė, D., Stonevičius, E., Karosienė, J., Savadova, K. and Kasperovičienė, J. (2018). Chlorophyll-a concentration retrieval in eutrophic lakes in Lithuania from Sentinel-2 data. *Geologija. Geografija*, *4*(1).

Guo, H., Huang J.J., Bowen Chen, B., Guo, X. and Singh, V.P. (2020). A machine learning-based strategy for estimating non-optically active water quality parameters using Sentinel-2 imagery. *International Journal of Remote Sensing*, 42(5), p.p.1841-1866.

Ha, N.T.T., Thao, N.T.P., Koike, K. and Nhuan, M.T. (2017). Selecting the best band ratio to estimate chlorophyll-a concentration in a tropical freshwater lake using sentinel 2A images from a case study of Lake Ba Be (Northern Vietnam). *ISPRS International Journal of Geo-Information*, *6*(9), p.290.

Hassan, G., Goher, M.E., Shaheen, M.E. and Taie, S.A. (2021). Hybrid Predictive Model for Water Quality Monitoring Based on Sentinel-2A L1C Data. *IEEE Access*, *9*, pp.65730-65749.

He, Y., Jin, S. and Shang, W. (2021). Water quality variability and related factors along the Yangtze River using Landsat-8. *Remote Sensing*, *13*(12), p.2241.

Hu, M., Ma, R., Cao, Z., Xiong, J. and Xue, K. (2021). Remote Estimation of Trophic State Index for Inland Waters Using Landsat-8 OLI Imagery. *Remote Sensing*, *13*(10), p.1988.

Huangfu, K., Li, J., Zhang, X., Zhang, J., Cui, H. and Sun, Q. (2020). Remote estimation of water quality parameters of medium-and small-sized inland rivers using Sentinel-2 imagery. *Water*, *12*(11), p.3124.

Jaiyeola, A.T. (2016). *Estimation of suspended sediment yield flowing into Inanda Dam using genetic programming* (Doctoral dissertation).

Karaoui, I., Arioua, A., Boudhar, A., Hssaisoune, M., El Mouatassime, S., Ouhamchich, K.A., Elhamdouni, D., Idrissi, A.E.A. and Nouaim, W. (2019). Evaluating the potential of Sentinel-2 satellite images for water quality characterization of artificial reservoirs: The Bin El Ouidane Reservoir case study (Morocco). *Meteorology Hydrology and Water Management. Research and Operational Applications*, *7*(1), pp.31-39.

Kim, H.H., Ko, B.C. and Nam, J.Y. (2016). Predicting chlorophyll-a using Landsat 8 OLI sensor data and the non-linear RANSAC method – a case study of Nakdong River, South Korea. *International Journal of Remote Sensing*, *37*(14), pp.3255-3271.

Kontopoulou, E., Kolokoussis, P. and Karantzalos, K. (2017). Water quality estimation in Greek lakes from Landsat 8 multispectral satellite data. *European Water*, *58*, pp.191-196.

Kurniadin, N. and Jaelani, L.M. (2016). Empirical Algorithm Modeling for Estimating Total Suspended Solid Concentration Using In-situ Data and Atmospheric Corrected Landsat 8, Case Study: Gili Iyang â€ TM s Waters Empirical Algorithm Modeling for Estimating Total Suspended Solid Concentration Us. In *The 2nd International Seminar on Science and Technology (ISST) for Sustainable Infrastructure Empowering Research and Technology for Sustainable Infrastructure* (pp. 379-380).

Kutser, T., Paavel, B., Verpoorter, C., Ligi, M., Soomets, T., Toming, K. and Casal, G. (2016). Remote sensing of black lakes and using 810 nm reflectance peak for retrieving water quality parameters of optically complex waters. *Remote Sensing*, *8*(6), p.497.

L3HARRIS GEOSPATIAL. (2013). Radiance vs. Reflectance. Available at: https://www.l3harrisgeospatial.com/Support/Self-Help-Tools/Help-Articles/Help-Articles-Detail/ArtMID/10220/ArticleID/19247/3377. (Accessed: 17 September 2021)

Lailia, N.L., Arafah, F., Jaelani, A. and Pamungkas, A.D. (2015). Development of water quality parameter retrieval algorithms for estimating total suspended solids and chlorophyll-A concentration using Landsat-8 imagery at Poteran island water. *Remote Sensing and Spatial Information Sciences*, *2*(2).

Larson, M.D., Simic Milas, A., Vincent, R.K. and Evans, J.E. (2021). Landsat 8 monitoring of multi-depth suspended sediment concentrations in Lake Erie's Maumee River using machine learning. *International Journal of Remote Sensing*, *42*(11), pp.4064-4086.

Ledesma, M.M., Bonansea, M., Ledesma, C.R., Rodríguez, C., Carreño, J. and Pinotti, L. (2019). Estimation of chlorophyll-a concentration using Landsat 8 in the Cassaffousth reservoir. *Water Supply*, *19*(7), pp.2021-2027.

Li, Y., Zhang, Y., Shi, K., Zhu, G., Zhou, Y., Zhang, Y. and Guo, Y. (2017). Monitoring spatiotemporal variations in nutrients in a large drinking water reservoir and their relationships with hydrological and meteorological conditions based on Landsat 8 imagery. *Science of the Total Environment*, *599*, pp.1705-1717.

Li, Y., Zhang, Y., Shi, K., Zhou, Y., Zhang, Y., Liu, X. and Guo, Y. (2018). Spatiotemporal dynamics of chlorophyll-a in a large reservoir as derived from Landsat 8 OLI data: understanding its driving and restrictive factors. *Environmental Science and Pollution Research*, *25*(2), pp.1359-1374.

Li, S., Song, K., Wang, S., Liu, G., Wen, Z., Shang, Y., Lyu, L., Chen, F., Xu, S., Tao, H., Du, Y., Fang, C. and Mu, G (2021a). Quantification of chlorophyll-a in typical lakes across China using Sentinel-2 MSI imagery with machine learning algorithm. *Science of The Total Environment*, *778*, p.146271.

Li, X., Ding, J. and Ilyas, N. (2021b). Machine learning method for quick identification of water quality index (WQI) based on Sentinel-2 MSI data: Ebinur Lake case study. *Water Supply*, *21*(3), pp.1291-1312.

Lillesand, T., Kiefer, R. W., and Chipman, J. (2000). *Remote sensing and image interpretation*. John Wiley & Sons.

Lim, J. and Choi, M. (2015). Assessment of water quality based on Landsat 8 operational land imager associated with human activities in Korea. *Environmental monitoring and assessment*. 187 (6), p.p.384.

Liu, H., Li, Q., Shi, T., Hu, S., Wu, G. and Zhou, Q. (2017). Application of sentinel 2 MSI images to retrieve suspended particulate matter concentrations in Poyang Lake. *Remote Sensing*, *9*(7), p.761.

Malahlela, O.E., Oliphant, T., Tsoeleng, L.T. and Mhangara, P. (2018). Mapping chlorophyll-a concentrations in a cyanobacteria-and algae-impacted Vaal Dam using Landsat 8 OLI data. *South African Journal of Science*, *114*(9-10), pp.1-9.

Manickum, T. (2020). Chemical Test Measurements for Potable Water Quality: A Preliminary Test Correlation Study in the Umgeni Water Catchments, Kwazulu-Natal, South Africa.

Manuel, A., Blanco, A.C., Tamondong, A.M., Jalbuena, R., Cabrera, O. and Gege, P. (2020). Optmization of bio-optical model parameters for turbid lake water quality estimation using Landsat 8 and wasi-2D. *The International Archives of Photogrammetry, Remote Sensing and Spatial Information Sciences*, *42*, pp.67-72.

Manzo, C., Bresciani, M., Giardino, C., Braga, F. and Bassani, C. (2015). Sensitivity analysis of a bio-optical model for Italian lakes focused on Landsat-8, Sentinel-2 and Sentinel-3. *European Journal of Remote Sensing*, *48*(1), pp.17-32.

Markogianni, V., Kalivas, D., Petropoulos, G. and Dimitriou, E. (2017). Analysis on the feasibility of Landsat 8 imagery for water quality parameters assessment in an oligotrophic Mediterranean Lake. *International Journal of Geological and Environmental Engineering*, *11*(9), pp.906-914.

Masocha, M., Dube, T., Nhiwatiwa, T. and Choruma, D. (2018). Testing utility of Landsat 8 for remote assessment of water quality in two subtropical African reservoirs with contrasting trophic states. *Geocarto international*, *33*(7), pp.667-680.

Mather, P. M. and Koch, M. (2011). *Computer processing of remotely-sensed images: an introduction*, 4th edition; John Wiley & Sons.

Matthews, M.W. (2011). A current review of empirical procedures of remote sensing in inland and near-coastal transitional waters. *International Journal of Remote Sensing*, *32*(21), pp.6855-6899.

Matthews, M.W. (2014). Eutrophication and cyanobacterial blooms in South African inland waters: 10 years of MERIS observations. *Remote Sensing of Environment*, *155*, pp.161-177.

Matthews, M.W. and Bernard, S. (2015). Eutrophication and cyanobacteria in South Africa's standing water bodies: A view from space. *South African journal of science*, *111*(5), pp.1-8.

Matongo, S., Birungi, G., Moodley, B. and Ndungu, P. (2015). Occurrence of selected pharmaceuticals in water and sediment of Umgeni River, KwaZulu-Natal, South Africa. *Environmental Science and Pollution Research*, *22*(13), pp.10298-10308.

Molkov, A.A., Fedorov, S.V., Pelevin, V.V. and Korchemkina, E.N. (2019). Regional models for high-resolution retrieval of chlorophyll a and TSM concentrations in the Gorky Reservoir by Sentinel-2 imagery. *Remote Sensing*, *11*(10), p.1215.

Mushtaq, F. and Nee Lala, M.G. (2017). Remote estimation of water quality parameters of Himalayan lake (Kashmir) using Landsat 8 OLI imagery. *Geocarto international*, *32*(3), pp.274-285.

Namugize, J.N., Jewitt, G. and Graham, M. (2018). Effects of land use and land cover changes on water quality in the uMngeni river catchment, South Africa. *Physics and Chemistry of the Earth, Parts A/B/C*, *105*, pp.247-264.

Ngabirano, H., Byamugisha, D. and Ntambi, E. (2016). Effects of seasonal variations in physical parameters on quality of gravity flow water in Kyanamira Sub-County, Kabale District, Uganda.

Ngetar, N.S. (2002). *Post-dam sediment dynamics below the Inanda Dam at the Mgeni estuary, KwaZulu-Natal (South Africa)* (Doctoral dissertation).

Nkoana, M.A. (2014). *Urban biodiversity management in the face of climate change: livelihood impacts and adaptation strategies in Inanda community of eThekwini Metropolitan Area, KwaZulu-Natal, South Africa* (Doctoral dissertation).

Olmanson, L.G., Page, B.P., Finlay, J.C., Brezonik, P.L., Bauer, M.E., Griffin, C.G. and Hozalski, R.M. (2020). Regional measurements and spatial/temporal analysis of CDOM in 10,000+ optically variable Minnesota lakes using Landsat 8 imagery. *Science of The Total Environment*, *724*, p.138141.

Ouma, Y.O., Noor, K. and Herbert, K. (2020). Modelling Reservoir Chlorophyll-a, TSS, and Turbidity Using Sentinel-2A MSI and Landsat-8 OLI Satellite Sensors with Empirical Multivariate Regression. *Journal of Sensors*, *2020*.

Palmer, S. C., Kutser, T. and Hunter, P. D. (2015). Remote sensing of inland waters: Challenges, progress and future directions. *Remote Sensing of Environment*, 157, p.p.1-8.

Patra, P.P., Dubey, S.K., Trivedi, R.K., Sahu, S.K. and Rout, S.K. (2017). Estimation of chlorophyll-a concentration and trophic states in Nalban Lake of East Kolkata Wetland, India from Landsat 8 OLI data. *Spatial Information Research*, *25*(1), pp.75-87.

Peterson, K.T., Sagan, V., Sidike, P., Cox, A.L. and Martinez, M. (2018). Suspended sediment concentration estimation from landsat imagery along the lower Missouri and middle Mississippi Rivers using an extreme learning machine. *Remote Sensing*, *10*(10), p.1503.

Peterson, K.T., Sagan, V. and Sloan, J.J. (2020). Deep learning-based water quality estimation and anomaly detection using Landsat-8/Sentinel-2 virtual constellation and cloud computing. *GIScience & Remote Sensing*, *57*(4), pp.510-525.

Pham, Q.V., Ha, N.T.T., Pahlevan, N., Oanh, L.T., Nguyen, T.B. and Nguyen, N.T. (2018). Using Landsat-8 images for quantifying suspended sediment concentration in Red River (Northern Vietnam) *remote sensing*, *10*(11), p.1841.

Pirasteh, S., Mollaee, S., Fatholahi, S.N. and Li, J. (2020). Estimation of phytoplankton chlorophyll-a concentrations in the Western Basin of Lake Erie using Sentinel-2 and Sentinel-3 data. *Canadian Journal of Remote Sensing*, *46*(5), pp.585-602.

Prasad, S., Saluja, R. and Garg, J.K. (2020). Assessing the efficacy of Landsat-8 OLI imagery derived models for remotely estimating chlorophyll-a concentration in the Upper Ganga River, India. *International Journal of Remote Sensing*, *41*(7), pp.2439-2456.

Pu, F., Ding, C., Chao, Z., Yu, Y. and Xu, X. (2019). Water-quality classification of inland lakes using Landsat 8 images by convolutional neural networks. *Remote Sensing*, *11*(14), p.1674.

Quang, N.H., Sasaki, J., Higa, H. and Huan, N.H. (2017). Spatiotemporal variation of turbidity based on landsat 8 oli in Cam Ranh Bay and thuy trieu lagoon, Vietnam. *Water*, *9*(8), p.570.

Rangeti, I. (2014). Determinants of Key Drivers for Potable Water Treatment Cost in uMngeni Basin. Master of Technology Thesis. *Environmental Health in the Faculty of Health Sciences, Durban University of Technology*.

Ritchie, J. C., Zimba, P. V. and Everitt, J. H. (2003) Remote sensing techniques to assess water quality. *Photogrammetric Engineering & Remote Sensing*, 69 (6), p.p.695-704.

Rodrigues, T., Alcântara, E., Watanabe, F. and Imai, N. (2017). Retrieval of Secchi disk depth from a reservoir using a semi-analytical scheme. *Remote Sensing of Environment*, *198*, pp.213-228.

Shang, Y., Liu, G., Wen, Z., Jacinthe, P.A., Song, K., Zhang, B., Lyu, L., Li, S., Wang, X. and Yu, X. (2021). Remote estimates of CDOM using Sentinel-2 remote sensing data in reservoirs with different trophic states across China. *Journal of Environmental Management*, *286*, p.112275.

Sharaf El Din, E.S. and Zhang, Y. (2017). Statistical estimation of the Saint John River surface water quality using Landsat-8 multi-spectral data. In *ASPRS Annual Conf. Proc. of Imaging and Geospatial Technology Forum (IGTF)*.

Sharaf El Din, E. "A novel approach for surface water quality modelling based on Landsat-8 tasselled cap transformation." *International Journal of Remote Sensing* 41, no. 18 (2020): 7186-7201.

Simpson, D. and Pillay, M. (2000). Quantifying externalities: Study of the impact of nutrient loading in the Msunduzi River on downstream users. In *WISA 2000 Biennial Conference, Sun City, South Africa* (pp. 2-4).

Soomets, T., Uudeberg, K., Jakovels, D., Brauns, A., Zagars, M. and Kutser, T. (2020). Validation and comparison of water quality products in baltic lakes using sentinel-2 msi and sentinel-3 OLCI data. *Sensors*, *20*(3), p.742.

Sòria-Perpinyà, X., Vicente, E., Urrego, P., Pereira-Sandoval, M., Ruíz-Verdú, A., Delegido, J., Soria, J.M. and Moreno, J. (2020). Remote sensing of cyanobacterial blooms in a hypertrophic lagoon (Albufera of València, Eastern Iberian Peninsula) using multitemporal Sentinel-2 images. *Science of the Total Environment*, *698*, p.134305.

Statistic Solutions. (2021). Correlation (Pearson, Kendall, Spearman). Available at: https://www.statisticssolutions.com/free-resources/directory-of-statistical-analyses/correlation-pearson-kendall-spearman/. (Accessed: 17 September 2021)

Tinmouth, N. (2009). *The Mgeni Estuary pre-and post Inanda Dam Estuarine dynamics* (Doctoral dissertation).

Toming, K., Kutser, T., Laas, A., Sepp, M., Paavel, B. and Nõges, T. (2016). First experiences in mapping lake water quality parameters with Sentinel-2 MSI imagery. *Remote Sensing*, *8*(8), p.640.

United States Geological Survey. (2021). Landsat 8. Available at: https://www.usgs.gov/core-science systems/nli/landsat/landsat8?qtscience_support_page_related_con=0#qtscience_support_page_related_con . (Accessed: 01 June 2021)

Vinh, P.Q., Ha, N.T.T., Binh, N.T., Thang, N.N., Oanh, L.T. and Thao, N.T.P. (2019). Developing algorithm for estimating chlorophyll-a concentration in the Thac Ba Reservoir surface water using Landsat 8 Imagery. *VIETNAM Journal of Earth Sciences*, *41*(1), pp.10-20.

Wang, H., Wang, J., Cui, Y. and Yan, S. (2021). Consistency of Suspended Particulate Matter Concentration in Turbid Water Retrieved from Sentinel-2 MSI and Landsat-8 OLI Sensors. *Sensors*, *21*(5), p.1662.

Watanabe, F.S.Y., Alcântara, E., Rodrigues, T.W.P., Imai, N.N., Barbosa, C.C.F. and Rotta, L.H.D.S. (2015). Estimation of chlorophyll-a concentration and the trophic state of the Barra Bonita hydroelectric reservoir using OLI/Landsat-8 images. *International journal of environmental research and public health*, *12*(9), pp.10391-10417.

Watanabe, F., Alcantara, E., Rodrigues, T., Rotta, L., Bernardo, N. and Imai, N. (2017). Remote sensing of the chlorophyll-a based on OLI/Landsat-8 and MSI/Sentinel-2A (Barra Bonita reservoir, Brazil). *Anais da Academia Brasileira de Ciências*, *90*, pp.1987-2000.

Yadav, S., Yamashiki, Y., Susaki, J., Yamashita, Y. and Ishikawa, K. (2019). Chlorophyll estimation of lake water and coastal water using landsat-8 and sentinel-2a satellite. *International Archives of the Photogrammetry, Remote Sensing & Spatial Information Sciences*.

Yang, Z. and Anderson, Y. (2016). Estimating chlorophyll-A concentration in a freshwater lake using Landsat 8 imagery. *J. Environ. Earth Sci*, *6*(4), pp.134-142.

Yanti, A., Susilo, B. and Wicaksono, P. (2016), November. The application of Landsat 8 OLI for total suspended solid (TSS) mapping in Gajahmungkur reservoir Wonogiri regency 2016. In *IOP Conference Series: Earth and Environmental Science* (Vol. 47, No. 1, p. 012028). IOP Publishing.

Yepez, S., Laraque, A., Martinez, J.M., De Sa, J., Carrera, J.M., Castellanos, B., Gallay, M. and Lopez, J.L. (2018). Retrieval of suspended sediment concentrations using Landsat-8 OLI satellite images in the Orinoco River (Venezuela). *Comptes Rendus Geoscience*, *350*(1-2), pp.20-30.

Zhang, Y., Zhang, Y., Shi, K., Zha, Y., Zhou, Y. and Liu, M. (2016). A Landsat 8 OLI-based, semianalytical model for estimating the total suspended matter concentration in the slightly turbid Xin'anjiang Reservoir (China). *IEEE journal of selected topics in applied earth observations and remote sensing*, *9*(1), pp.398-413.

Zhang, T., Huang, M. and Wang, Z. (2020). Estimation of chlorophyll-a Concentration of lakes based on SVM algorithm and Landsat 8 OLI images. *Environmental Science and Pollution Research*, *27*(13), pp.14977-14990.